

The KMT2D Kabuki syndrome histone methylase
controls neural crest cell differentiation and facial morphology

Karl B. Shpargel^{1,3}, Cassidy L. Mangini¹, Guojia Xie², Kai Ge², Terry Magnuson¹

¹Department of Genetics and Lineberger Comprehensive Cancer Center, University of North Carolina, Chapel Hill, NC 27599-7264, USA

²Laboratory of Endocrinology and Receptor Biology, National Institute of Diabetes and Digestive and Kidney Diseases, National Institutes of Health, Bethesda, MD 20892, USA

³Corresponding Author: shpargel@email.unc.edu

Key Words: KMT2D, MLL4, Kabuki syndrome, histone methylation, neural crest, craniofacial

Summary

Chromatin-modifying enzymes are mutated in a wide array of craniofacial disorders. We contrast KMT2D and UTX neural crest differentiation function as sources of variation in facial gestalt for Kabuki syndrome.

Abstract

Kabuki syndrome (KS) is a congenital craniofacial disorder resulting from mutations in the KMT2D histone methylase (KS1) or the UTX histone demethylase (KS2). With small cohorts of KS2 patients, it is not clear if differences exist in clinical manifestations relative to KS1. We mutated KMT2D in neural crest cells (NCCs) to study cellular and molecular functions in craniofacial development with respect to UTX. Similar to UTX, KMT2D NCC knockout mice demonstrate hypoplasia with reductions in frontonasal bone lengths. We have traced the onset of KMT2D and UTX mutant NCC frontal dysfunction to a stage of altered osteochondral progenitor differentiation. KMT2D NCC loss of function does exhibit unique phenotypes distinct from UTX mutation including fully penetrant cleft palate, mandible hypoplasia, and deficits in cranial base ossification. KMT2D mutant NCCs lead to defective secondary palatal shelf elevation with reduced expression of extracellular matrix components. KMT2D mutant chondrocytes in the cranial base fail to properly differentiate leading to defective endochondral ossification. We conclude that KMT2D is required for appropriate cranial NCC differentiation and KMT2D specific phenotypes may underlie differences between Kabuki syndrome subtypes.

Introduction

Epigenetics play a vital role in facial development as mutations in chromatin-modifying enzymes have been discovered to underlie syndromic craniofacial disorders (Berdasco and Esteller, 2013; Ng et al., 2010; Lederer et al., 2012; Tsurusaki et al., 2012; Santen et al., 2012; Vissers et al., 2004; Petrij et al., 1995; Roelfsema et al., 2005; Sanka et al., 2007). These chromatin regulatory enzymes function by catalyzing the addition or removal of histone post-translational modifications or by remodeling nucleosomes. These activities will alter DNA accessibility and influence the binding of transcriptional activation or repression complexes. Disorders from mutations in chromatin modifying factors can have overlapping clinical features (Bramswig et al., 2015; Negri et al., 2019; Sakata et al., 2017; Schulz et al., 2014; Verhagen et al., 2014), indicating that they may have co-regulatory functions in facial development. Kabuki syndrome is a craniofacial disorder that manifests from mutations in two distinct histone modifying enzymes and represents a unique disorder that may be dependent on co-regulatory chromatin-modifier function.

Kabuki syndrome is a congenital disorder distinguished by facial dysmorphology, intellectual disability, skeletal and dermatoglyphic abnormalities, developmental delay, and postnatal growth deficits (Adam et al., 1993; Kuroki et al., 1981; Niikawa et al., 1981; Niikawa et al., 1988). Kabuki patients exhibit distinctive facial hypoplasia with a depressed nasal tip, cleft or high arched palate, lower eyelid eversion, high arched eyebrows, elongated palpebral fissures, and prominent ears. The craniofacial components of the disorder can be accompanied by a variety of cardiac defects.

Kabuki syndrome is genetically heterogeneous. Mutations were initially and have been most frequently identified in KMT2D (mutated in 39%-74% of cases), a histone H3 Lysine 4 (H3K4) methylase (Banka et al., 2015; Bogershausen et al., 2016; Cocciadiferro et al., 2018; Hannibal et al., 2011; Makrythanasis et al., 2013; Micale et al., 2011; Miyake et al., 2013; Ng et al., 2010). This predominant molecular subtype has been termed type 1 Kabuki syndrome (KS1). A smaller percentage of Kabuki patients (3-6%) exhibit mutations in UTX (KDM6A), an X-chromosomal histone H3 Lysine 27 (H3K27) demethylase and are classified as KS2 (Lederer et al., 2012; Miyake et al., 2013; Banka et al., 2015; Bogershausen et al., 2016; Cocciadiferro et al., 2018). KMT2D and UTX form a biochemical protein complex and

thus may function at common sites in the genome (Cho et al., 2007). However, it is not clear if phenotypic differences exist between KS1 and KS2 patients. Overall, KMT2D mutant patients more frequently demonstrate classical facial dysmorphism compared to patients with other genetic lesions (Adam et al., 2019; Makrythanasis et al., 2013). In large cohort analyses, KMT2D mutant KS1 patients are reported to have more consistent, typical facial dysmorphology and hypotonia while UTX mutant KS2 patients have more prominent short stature and growth deficiencies (Banka et al., 2015; Miyake et al., 2013). Additionally, cleft palate is much more prevalent with KMT2D mutations compared to UTX (Adam et al., 2019). In contrast, other reports have described KS2 patients as having classical facial phenotypes with no distinction between UTX or KMT2D mutation (Bogershausen et al., 2016).

Neural crest cells (NCCs) comprise a multipotent stem cell population that gives rise to anterior cranial structures (Jiang et al., 2002; McBratney-Owen et al., 2008). Cranial NCCs are specified in the dorsal neural tube, migrate in streams to anterior facial regions for differentiation towards osteoblast and chondrocyte lineages that will develop bone and cartilage (Dupin et al., 2006; Santagati and Rijli, 2003; Trainor, 2005). Throughout specification, migration, and differentiation, NCCs undergo drastic alterations in transcriptional states that can be dependent on epigenetic regulation (Bajpai et al., 2010; Hu et al., 2014; Minoux et al., 2017; Rada-Iglesias et al., 2012; Strobl-Mazzulla et al., 2012). For these reasons, NCC specific knockouts have been utilized to model the function of chromatin-modifying enzymes in craniofacial disorders (Chandler and Magnuson, 2016; Li et al., 2013; Sperry et al., 2014).

We have previously examined the function of UTX in mouse craniofacial development through NCC specific knockout approaches (Shpargel et al., 2017). We utilized a *Wnt1-Cre* transgene to drive NCC specific mouse knockout of a conditional floxed (*fl*) *Utx* allele. Homozygous *Utx^{fl/fl} Wnt1-Cre* conditional female NCC knockout mice (*Utx^{cFKO}*) exhibited severe frontonasal hypoplasia and growth deficiencies, as well as reduced viability prior to weaning. Hemizygous *Utx^{fl/y} Wnt1-Cre* male mice (*Utx^{cMKO}*) were viable with mild facial hypoplasia and moderate postnatal growth deficiencies compared to *Utx^{cFKO}* due to partial redundancy between UTX and the Y-chromosomal homolog, UTY (Shpargel et al., 2012; Shpargel et al., 2017). Mouse UTX NCC knockout modeled several dysmorphic facial phenotypes observed in human Kabuki syndrome.

We now establish NCC knockout of KMT2D for comparison of craniofacial anatomical and NCC cellular phenotypes to UTX loss of function. We find that heterozygous loss of KMT2D in NCC lineages resulted in mild facial hypoplasia and deficiencies in postnatal growth while homozygous deletion of NCC KMT2D manifested in perinatal lethality. KMT2D NCC knockout phenocopied the frontonasal hypoplasia previously observed with UTX deletion. Although KMT2D mutant NCCs displayed appropriate specification and migration, frontal bone ossification centers displayed altered distributions of NCC osteoblast and chondrocyte differentiation for both KMT2D and UTX loss of function. In contrast, fully penetrant secondary cleft palate, mandible hypoplasia, and cranial base ossification phenotypes only manifested with KMT2D NCC mutation. NCC KMT2D knockout palatal shelves failed to elevate with altered expression of extracellular matrix components. Within the cranial base, KMT2D knockout produced deficiencies in endochondral ossification of presphenoid and basisphenoid bone due to loss of NCC hypertrophic chondrocyte differentiation. Our results highlight KMT2D function in several aspects of cranial NCC differentiation and identify developmental differences in KMT2D and UTX requirements that may underlie reported KS1 and KS2 phenotypic disparity.

Results

Establishment of a KMT2D conditional null allele

We obtained a *Kmt2d* conditional allele with floxed exons upstream of the SET methylase domain for conditional knockout approaches (Figure 1A). Cre mediated deletion will frameshift the coding sequence to a stop codon creating a mutant KMT2D protein lacking SET and methylase activity. We utilized a *Vasa-Cre* transgene to generate a germline knockout of the KMT2D SET domain. KMT2D SET domain knockout embryos were dead and resorbed by E11.5 (4/4 embryos), similar to published *Kmt2d* null alleles (Lee et al., 2013). Primary MEFs isolated from a pool of E9.5 embryos carrying the KMT2D SET deletion revealed an absence of KMT2D protein in the expected size range for SET deletion (568 kD, Figure 1B), consistent with findings that the SET domain is essential for KMT2D protein stability (Jang et al., 2019).

KMT2D NCC knockout models Kabuki facial dysmorphism

To model the craniofacial dysfunction of KMT2D in Kabuki syndrome, the mouse *Kmt2d* conditional allele was crossed with the NCC specific *Wnt1-Cre* transgene (Danielian et al., 1998). Heterozygous conditional *Kmt2d^{+/fl} Wnt1-Cre* mice (*Kmt2d^{chHet}*) were viable but exhibited facial dysmorphism (Figure 1C-D) and postnatal growth deficiency (Figure 1E). The Kabuki-like facial features such as depressed snout, broad face, dome shaped forehead, ocular phenotypes, and abnormal, rounded ears were fully penetrant. These NCC KMT2D haploinsufficient facial deformities phenocopy *Utx^{CMKO}* mice (Shpargel et al., 2017).

To understand KMT2D NCC requirements, we examined the phenotypic effects of completely removing KMT2D protein. *Kmt2d^{fl/fl} Wnt1-Cre* mice (*Kmt2d^{CKO}*) died at birth as no pups were observed at postnatal day 2 (P2) while 8 were expected by Mendelian genetics. At P1, *Kmt2d^{CKO}* pups demonstrated severe facial hypoplasia (Figure 1F, H) relative to WT controls (*Kmt2d^{fl/fl}* without *Cre*). In contrast, *Kmt2d^{chHet}* pups had more intermediate dysplasia (Figure 1G). Quantification of facial characteristics such as a reduction in the nose to ear length (Figure 1I) and frontal angle (Figure 1J) highlighted the shortened frontonasal structures present in *Kmt2d^{chHet}* and *Kmt2d^{CKO}* newborn pups and the graded dysmorphism that is dependent on KMT2D dosage.

Whole mount alizarin red and alcian blue staining for bone/cartilage in *Kmt2d^{CKO}* pups (Figure 2A-B) facilitated quantitation of bone structure (Figure 2C). *Kmt2d^{CKO}* resulted in significant reductions in nasal and frontal bone lengths, but had no effect on parietal bone, which is derived from non-neural crest mesoderm (Jiang et al., 2002). *Kmt2d^{chHet}* pups exhibited intermediate reductions in nasal and frontal bone lengths (with frontal bone measurements lacking statistical significance from WT). While this compilation of craniofacial phenotypes was similar to *Utx^{CFKO}* (Shpargel et al., 2017), *Kmt2d^{CKO}* exhibited mandible hypoplasia that was not as severely affected in *Utx^{CFKO}* at birth (Figure 2D-F). *Kmt2d^{CKO}* mandibles had particularly underdeveloped condylar process with a lack of condylar cartilage (Figure 2E, asterisk).

KMT2D controls post-migratory NCC function

We traced NCC development to identify the stage at which *Kmt2d^{cko}* frontal NCCs display an altered phenotype. Mouse cranial NCCs are specified in the dorsal neural tube at embryonic day 7.5-8 (E7.5-E8) and complete migration to anterior facial positions at approximately E9 (Serbedzija et al., 1992). Across subsequent post-migratory development (E11.5-E13.5), cranial NCCs experience dramatic changes in cellular properties such as proliferation and differentiation. NCC lineage tracing was performed with a Cre inducible tomato fluorescent reporter (Madisen et al., 2010). At post-migratory cranial NCC timepoints (E11.5 and E13.5), *Kmt2d^{cko}* embryos demonstrated similar anterior NCC positioning and fluorescent intensity as WT (*Kmt2d^{+/+}* with *Wnt1-Cre*) controls (Figure 3A-F and Figure S1A-B).

SOX10 is a transcription factor that becomes expressed in all NCCs during migration, but persists in the peripheral nervous system and melanocyte lineages upon migratory completion (Hari et al., 2012; Kuhlbrodt et al., 1998; Southard-Smith et al., 1998). We performed whole mount *in situ* hybridization for *Sox10* expression to examine migratory NCCs in *Kmt2d^{cko}* embryos (Figure S1C-D). At E10.5, NCC migration had completed normally in both WT and *Kmt2d^{cko}* embryos, as there were no lagging Sox10 positive cells in the migratory streams expected from cranial NCCs (Serbedzija et al., 1992). Furthermore, *Sox10* expression domains in post-migratory peripheral nervous system components such as trigeminal and dorsal root ganglia appeared normal in *Kmt2d^{cko}* embryos. Therefore, cranial NCC specification and migration appeared largely normal in *Kmt2d^{cko}* embryos.

We utilized a second Cre driver with more specificity to remove KMT2D function at the completion of migration. Although SOX10 is expressed in migrating NCCs, a *Sox10-Cre* transgene has been established (Matsuoka et al., 2005) that does not induce recombination until the completion of migration. Reporter based analyses have demonstrated that *Sox10-Cre* activity is delayed compared to endogenous *Sox10* expression and is absent from early migrating NCCs (Hari et al., 2012; Jacques-Fricke et al., 2012). In contrast to *Wnt1-Cre*, *Sox10-Cre* reporter staining was low in migratory cranial NCCs streams and became activated upon reaching anterior destinations. Upon crossing to this *Sox10-Cre* transgene, the tomato reporter demonstrated localization restricted to anterior cranial regions

characteristic of migrated NCCs (Figure S1E-F) and lacked the posterior neural tube and midbrain localization characteristic of *Wnt1-Cre* activity (Figure 3E). *Sox10-Cre* had a similar efficiency in differentiating NCCs (Figure S1G-H) as *Wnt1-Cre* (Figure S1A). *Sox10-Cre* driven *Kmt2d* knockout (*Kmt2d*^{cS10KO}) produced frontonasal hypoplasia (Figure 3G-J) similar to *Wnt1* driven *Kmt2d*^{cKO} mutagenesis. Skeletal staining also demonstrated consistent reductions in frontal, nasal, and mandible bone length in *Kmt2d*^{cS10KO} pups at birth (Figure 3K-Q). We conclude that the craniofacial phenotypes in *Kmt2d*^{cKO} pups manifest from KMT2D loss of function in post-migratory cranial NCCs.

KMT2D regulates frontal osteochondral differentiation

Provided that the cranial NCC distribution appeared normal at E13.5 early differentiation timepoints (Figure 3D-F), we examined NCC differentiation events that precede intramembranous ossification of the frontal bone. Frontal bone primordia are specified in supraorbital regions of the head, basolateral to the brain (Ishii et al., 2003; Yoshida et al., 2008). Cranial NCC mesenchymal cells within the supraorbital arch differentiate to osteoblast lineages that are required for the synthesis and mineralization of frontal bone (Ferguson and Atit, 2019; Ishii et al., 2003). In this differentiation pathway (depicted in Figure 4A), SOX9 expressing ectomesenchymal stem cells initiate RUNX2 expression in an osteochondral progenitor cell that has potential to differentiate to pre-osteoblasts expressing RUNX2 or pre-chondrocytes expressing SOX9 (Bhatt et al., 2013). Committed differentiation to osteoblast lineages requires RUNX2 induced Osterix (OSX) expression (Nakashima et al., 2002), while SOX9 expressing pre-chondrocytes will induce downstream targets such as type II collagen (COL2). We examined KMT2D function in cranial NCC differentiation towards pre-osteoblast and pre-chondrocyte lineages by immunofluorescence for RUNX or COL2 respectively on E13.5 supraorbital coronal sections. In the E13.5 frontal ossification center, WT pre-osteoblast and pre-chondrocyte lineages have diverged with COL2+ pre-chondrocytes specified medially and RUNX2+ pre-osteoblasts occupying a lateral crescent domain (Figure 4B) similar to previous reports (Goodnough et al., 2012; Ishii et al., 2003; Vivatbutsiri et al., 2008). *Kmt2d*^{cKO} embryos have specified these lineages, however the RUNX2+ osteoblast domain (Figure 4B-C) and OSX+ committed pre-osteoblasts (Figure 4D-E) are positioned more laterally compared to WT. The *Kmt2d*^{cKO} medial

chondrocyte domain has extended laterally indicating that some osteochondral progenitor differentiation in this region may have instead skewed towards the chondrocyte lineage.

Unlike *Kmt2d*^{cko}, *Utx*^{cko} frontonasal NCCs experience an increase in apoptosis at the onset of E13.5 differentiation timepoints (Shpargel et al., 2017). We analyzed *Utx*^{cko} frontal primordia to identify if UTX knockout produced an altered pattern of osteochondral differentiation similar to KMT2D. *Utx*^{cko} cranial NCCs within the supraorbital arch had a laterally shifted pattern of osteoblast and chondrocyte differentiation similar to *Kmt2d*^{cko} as both RUNX2+ and committed OSX+ osteoblasts were restricted to more lateral domains compared to WT (Figure 4F-I). In frontal primordia, *Kmt2d* was expressed throughout both osteoblasts and chondrocytes but demonstrated elevated osteoblast expression (Figure S2A) supporting a function in differentiation. UTX expression localized to both chondrocytes and osteoblasts with no tissue specific bias (Figure S2B-C). The patterns of altered *Kmt2d*^{cko} osteoblast differentiation persisted at later E15.5 stages and led to altered frontal bone shape (Figure S3A-B). While the areas of the specified RUNX2+ osteoblast and committed OSX+ osteoblast domains were not impacted by KMT2D NCC knockout (Figure 4J), the length of the RUNX2+ domain was shorter (Figure 4K) and the position of the osteoblast domains was consistently altered across *Kmt2d*^{cko} embryos (Figure 4L). We examined earlier E12.5 stages when frontal primordia are becoming specified. At this stage of development osteochondral progenitor cells have diverged into RUNX2+ pre-osteoblasts and SOX9+ pre-chondrocytes, however pre-osteoblasts lack OSX expression characteristic of lineage commitment (Figure S3C-F). At this earlier stage the osteoblast/chondrocyte domains appear similar in WT and *Kmt2d*^{cko} embryos (Figure S3C-D). A 2-hour BrdU injection prior to dissection indicated normal patterns of proliferation in E12.5 *Kmt2d*^{cko} frontal primordia (Figure S3G-I) with a lack of apoptosis as indicated by cleaved Caspase 3 signal (Figure S3J-K). Therefore, the *Kmt2d*^{cko} frontal phenotypes arise from altered patterns of osteochondral differentiation as these domains expand at E13.5.

KMT2D is required for morphogenesis in secondary palatogenesis

KMT2D mutant KS1 human patients have a higher incidence of cleft palate compared to UTX mutation (Adam et al., 2019). Therefore, we assessed palatogenesis in *Kmt2d^{cko}* embryos. In contrast to *Utx^{cko}* pups that demonstrate a low penetrance of cleft palate (Shpargel et al., 2017), *Kmt2d^{cko}* embryos had fully penetrant cleft palate that likely contributes to postnatal lethality (Figure 5A-B). Similarly, *Kmt2d^{cs10ko}* embryos (Figure 3H) demonstrated fully penetrant cleft palate (4/4 embryos).

Secondary palate formation is a highly organized process involving outgrowth of the palatal shelf from the maxillary prominence (E11.5-E12.5), vertical outgrowth and remodeling to elevate the shelves above the tongue to a horizontal position (E12.5-E14.5), and midline fusion of the shelves with degeneration of the epithelial seam (E14.5-E15.5) to form a continuous palate (Bush and Jiang, 2012). We examined the NCC cellular and molecular mechanisms of dysfunctional palatogenesis in *Kmt2d^{cko}* embryos. Compared to WT, E13.5 *Kmt2d^{cko}* embryos lacked vertical outgrowth and extension of the distal tip of the anterior palatal shelf (Figure 5C-D). Notably, the tongue in *Kmt2d^{cko}* embryos is situated more posterior relative to the anterior palatal domain and may play a role in defective *Kmt2d^{cko}* elevation. As failed outgrowth and elevation may also result from deficient palatal shelf mesenchymal proliferation, we labeled mitotic cells by immunofluorescence for pH3S10 (Figure 5C-D). Overall, there was a similar distribution of mitotic cells in WT and *Kmt2d^{cko}* palatal shelves (Figure 5G).

Palatal morphogenesis is also dependent on NCC mesenchymal remodeling and condensation in the interior side of the palatal shelf which is accompanied by appropriate levels of osteogenic differentiation (Fu et al., 2017; Jin et al., 2010; Wu et al., 2008). In WT E13.5 sections, the interior palatal mesenchymal cells express RUNX2, have condensed, and have differentiated to committed OSX+ osteoblasts (Figure 5E). In contrast, *Kmt2d^{cko}* palatal shelves are deficient in OSX+ differentiation (Figure 5F, H). To understand the molecular mechanisms underlying KMT2D function in palatogenesis, we dissected E14.25 WT and *Kmt2d^{cko}* palatal shelves prior to fusion and performed RNA-seq to identify mis-expressed genes and pathways. A total of 252 genes were significantly reduced in expression in *Kmt2d^{cko}* samples with 161 genes upregulated (Supplemental Table 1), consistent with

KMT2D function in gene activation events. Further refinement of this list for genes that have higher levels of WT palate expression (RPKM > 2) with more dramatic *Kmt2d^{cko}* expression changes (logFC < -1) yielded a set of 115 KMT2D affected genes (Supplemental Table 1: Sheet 3). Both gene set enrichment analysis (Broad MSigDB) and Ingenuity Pathway Analysis identified that *Kmt2d^{cko}* downregulated genes were most significantly enriched for factors in extracellular matrix organization (Figure 5I, Supplemental Table 1: Sheet 4). Induction of extracellular matrix (ECM) components are a feature of remodeling mesenchymal cells within the interior vertical palatal shelf (Chiquet et al., 2016; Jin et al., 2010). We find that many matrix remodeling components such as collagens, collagen processing factors, and extracellular glycoproteins are consistently reduced in expression with KMT2D loss of function (Figure S4A and supplemental Table 1).

We examined the spatial distribution of ECM components by picrosirius red histological stain which has an affinity for matrix collagen. At E14.25, picrosirius red ECM stain was enriched at differentiating osteoblasts within the interior of WT palatal shelves as well as mesenchymal supporting cells layered underneath regions of epithelial folding that form the distal palatal tip (Figure 5J). These ECM enrichments were lacking in *Kmt2d^{cko}* embryos (Figure 5K) that coincided with an abnormally shaped distal extension. Although the overall area of these extensions was similar (Figure S4B), WT palatal shelves exhibited a longer extension than *Kmt2d^{cko}* (Figure 5L). BrdU labeling in E14.25 embryos demonstrated similar proliferation within these extensions (Figure S4C-E) and cleaved Caspase 3 immunofluorescence revealed very few apoptotic cells in either WT or *Kmt2d^{cko}* palatal shelves (Figure S4F-G). Examination of initial palatal shelf outgrowth from the maxillary prominence at E12.5 revealed inconsistent phenotypes with a lack of *Kmt2d^{cko}* proliferative or apoptotic defects (Figure S4H-P). The area and length of the *Kmt2d^{cko}* palatal shelf outgrowth was slightly smaller but failed to reach statistical significance (Figure S4J-K).

Tmem119, one of the most significantly downregulated genes in *Kmt2d^{cko}* palatal shelves (supplemental Table 1), is known to function in osteoblast differentiation (Hisa et al., 2011). In WT embryos, TMEM119 was highly expressed throughout the interior palate in regions of differentiating osteoblasts but was also localized more diffusely through distal extensions (Figure 5M). TMEM119 expression was lost throughout the *Kmt2d^{cko}* palatal shelves (Figure 5N). Other ECM regulatory

genes identified by *Kmt2d*^{ckO} RNA-seq were also elevated in osteoblast differentiation (*Col8a2* and *Pcolce*) or in distal palatal extensions (*Col8a2*) with reduced *Kmt2d*^{ckO} expression (Figure 5O-R) highlighting a role for KMT2D in these processes. *Kmt2d* expression was elevated in both osteoblast differentiation domains and mesenchymal cells in the vicinity of epithelial folds (Figure S2F), regions that correlated with transcripts misregulated in *Kmt2d*^{ckO} palatal shelves. We hypothesized that perhaps redundancy between UTX and another H3K27 demethylase, KDM6B (JMJD3), are the reason for low cleft palate penetrance in *Utx*^{ckO} embryos (Shpargel et al., 2017). UTX was expressed throughout the palatal mesenchyme with enrichment in distal and subepithelial regions (Figure S2G-H). KDM6B expression demonstrated similar subepithelial localization but was also upregulated with osteoblast differentiation in the palate (Figure S2I-J) as well as the supraorbital ridge (Figure S2D-E). Therefore, redundancy between H3K27 demethylases may lead to observed *Kmt2d*^{ckO} and *Utx*^{ckO} phenotypic differences.

KMT2D regulates NCC endochondral ossification in the cranial base

The nasal and maxillary components of the viscerocranium (facial skeleton) and calvaria portion (including the frontal bone) of the neurocranium (brain case) are formed directly through osteoblast dependent intramembranous ossification. In contrast, within the cranial base (basicranium) support of the neurocranium, bone is deposited through endochondral ossification in the presence of cartilage and directed by chondrocyte differentiation. As the anterior cranial base is NCC derived (McBratney-Owen et al., 2008; Szabo-Rogers et al., 2010) and the cranial base provides structural support for the viscerocranium to influence facial morphology (Lieberman et al., 2000; Neaux et al., 2018; Nie, 2005), we examined whether these structures were properly formed in *Kmt2d*^{ckO} newborn pups.

We performed alizarin red and alcian blue staining for bone/cartilage on postnatal WT and *Kmt2d*^{ckO} pups at birth for whole mount imaging of the basicranium (Figure 6A-B). Whereas the WT cranial base has ossification of both the presphenoid and basisphenoid bones at birth, *Kmt2d*^{ckO} pups demonstrated an absence of presphenoid bone deposition and a shortened, abnormally shaped basisphenoid bone. In addition, *Kmt2d*^{ckO} pups exhibited underdeveloped pterygoid processes, palatine, and tympanic structures. Hyoid bone ossification, also dependent on NCC based endochondral ossification, was also absent in *Kmt2d*^{ckO}

pups and only stained for alcian blue cartilage. Additionally, the mandibular condylar process hypoplasia (Figure 2E) is due to a lack of endochondral ossification from the condylar cartilage. Postoptic roots of the *Kmt2d^{ckO}* sphenoid bone (lesser wings) were ossified (Figure 6B), however these structures form from mesoderm derived hypochiasmatic cartilage (McBratney-Owen et al., 2008). In contrast, *Utx^{ckO}* pups demonstrated proper formation of all basicranial structures even in instances of cleft palate where the palatine bone has not fused at the midline (Figure 6C). *Kmt2d^{ckS10KO}* embryos with loss of function in post-migratory NCCs had identical cranial base phenotypes to *Wnt1-Cre* based knockout with the exception that these pups on occasion displayed a small strip of presphenoid bone formation that was greatly reduced compared to WT (Figure 6D and S5A). Quantitation of whole mount bone lengths along the cranial base midline further illustrates the reductions in basisphenoid and presphenoid bone development in both *Kmt2d^{ckHet}* and *Kmt2d^{ckO}* skeletal preparations (Figure 6E). Notably, the length of the presphenoidal synchondrosis, the intermediary cartilage responsible for formation of basisphenoid and presphenoid bone was not altered in the *Kmt2d^{ckHet}* cranial base.

Due to deficiencies in cranial base endochondral ossification, we performed sagittal sections through the midline of this cranial region to analyze chondrocyte histology. Basicranial bones are formed at ossification centers surrounded by cartilage. The synchondroses (cartilaginous joints) between basicranial ossification centers have bidirectional growth for ossification at opposing ends of the growth plate. The spheno-occipital synchondrosis is the growth center for both the basioccipital and basisphenoid bones (Figure 7A). The basisphenoid bone will form at the junction of the spheno-occipital and presphenoidal (intersphenoid) synchondroses. The presphenoid bone will form at the junction of the presphenoidal synchondrosis and the septopresphenoidal junction, posterior to the nasal septum.

The synchondroses have zones of resting, proliferative, and hypertrophic chondrocyte differentiation (Figure 7A). Following chondrocyte hypertrophy, osteoblasts will differentiate from the perichondrium surrounding the cartilage anlage, populate the ossification zone, and synthesize bone. In contrast to the WT presphenoid bone, which is ossified at birth, *Kmt2d^{ckO}* sections have an absence of presphenoid bone synthesis and a reduction in the length of chondrocyte hypertrophic zones at this site (Figure 7C, G). We quantified the overall length of the hypertrophic zone from both the anterior (septopresphenoidal) and posterior

(presphenoidal synchondrosis) growth zones for the presphenoid as well as the proliferative zone from the presphenoidal synchondrosis. *Kmt2d^{cko}* chondrocytes had a normal proliferative zone but had significant reductions in the amount of hypertrophic differentiation and an absence of bone deposition (Figure 7N). *Kmt2d^{ch}* chondrocytes had an intermediate phenotype (Figure 7E). Differentiated presphenoid *Kmt2d^{cko}* chondrocytes were not as hypertrophic with significant decreases in cell area (Figure 7O-Q). As *Utx^{cko}* pups demonstrated presphenoid ossification (Figure 6C), we examined if UTX is expressed throughout these cell types. UTX was expressed throughout presphenoidal chondrocytes and osteoblasts (Figure S2K-L), in a similar fashion to KDM6B (Figure S2M-N) which may be redundant to UTX.

Within the *Kmt2d^{cko}* basisphenoid ossification zone, the anterior growth zone (presphenoidal synchondrosis side) similarly had significant reductions in chondrocyte hypertrophic differentiation and bone deposition (Figure 7B, D, F, N). However, the effect on the *Kmt2d^{cko}* basisphenoid ossification zone was not nearly as severe as the presphenoid. We performed NCC lineage tracing with the Cre responsive tomato reporter to examine the contributions of mutant cells to these structures (Figure 7H-M). In both WT (with *Wnt1-Cre*) and *Kmt2d^{ch}*, tomato positive NCC lineages contribute to both the anterior and posterior chondrocyte growth zones surrounding the presphenoid in addition to the RUNX2 highly expressing osteoblasts within the bone matrix (Figure 7I, K). In contrast, only the anterior basisphenoid growth zone and perichondrium are comprised of NCC lineages, yet osteoblasts within the basisphenoid matrix are almost entirely NCC derived (Figure 7H, J). The *Kmt2d^{cko}* basisphenoid bone was instead comprised of a mix of NCC and non-NCC lineages (Figure 7L). Therefore, the deficiencies in *Kmt2d^{cko}* NCC chondrocyte hypertrophy within the basisphenoid anterior growth zone (Figure 7N) can be compensated by the posterior spheno-occipital synchondrosis that has been reported to be partially comprised of mesoderm lineages (McBratney-Owen et al., 2008).

Discussion

Kabuki syndrome is a genetically heterogeneous craniofacial syndrome largely resulting from mutations in *KMT2D* and *UTX*, but rare mutations have also been identified in a small subset of other genes (Lintas and Persico, 2018). Clinical diagnosis of Kabuki syndrome is ascribed to a distinct facial gestalt, however the cellular mechanisms underlying altered craniofacial development are largely unknown. The disorder has been modeled in other organisms through whole animal loss of function approaches. Knockdown or knockout of *KMT2D* or *UTX* in zebrafish produced branchial arch and viscerocranium hypoplasia with altered cartilage structures (Bögershausen et al., 2015; Van Laarhoven et al., 2015). Morpholino knockdown in *Xenopus* embryos resulted in craniofacial and cartilaginous deformities (Schwenty-Lara et al., 2019). Mouse homozygous *Kmt2d* knockout leads to early embryonic lethality (Lee et al., 2013) that precludes analysis of Kabuki dependent phenotypes. Heterozygous *Kmt2d* mutations have been used to model the neurological, cardiac, and skeletal components of Kabuki syndrome (Ang et al., 2016; Björnsson et al., 2014; Carosso et al., 2019; Fahrner et al., 2019).

We now demonstrate by mouse tissue specific approaches that *KMT2D* function intrinsic to neural crest cells is essential for appropriate craniofacial development. While early NCC developmental processes such as specification and migration appear grossly normal, we observe NCC dependency on *KMT2D* for appropriate differentiation in several structural components within anterior cranial tissues. Intramembranous ossification of the frontal bone is dependent on localized osteoblast differentiation from osteochondral progenitors. NCC *KMT2D* loss of function leads to mild reductions and altered distributions of these pre-osteoblast domains in frontal primordia with expansion of pre-chondrocyte differentiation. Alternatively, within the basicranium, *KMT2D* functions in terminal differentiation of hypertrophic chondrocytes and is essential in formation of bone derived by endochondral ossification. *KMT2D* is essential in palatogenesis and NCC loss of function leads to altered mesenchymal differentiation with altered expression of extracellular matrix components. While we did not observe any significant changes in proliferation or apoptosis of these progenitor domains, it is possible that subtle regions specific changes might contribute to the observed phenotypes. Consistent with our findings, regional mesenchymal condensation as well as expression of extracellular matrix collagens, processing factors, and glycoproteins are essential in

palatal shelf elevation (Chiquet et al., 2016; d'Amaro et al., 2012; Jin et al., 2010; Logan et al., 2019; Zhang et al., 2015b). We find that several of the KMT2D transcriptional targets are expressed in osteoblast differentiation domains and folding subepithelial mesenchyme that may shape the distal palatal shelf (Yu and Ornitz, 2011).

KMT2D has previous ascribed functions in cellular differentiation events. KMT2D cooperated with lineage determining transcription factors to catalyze H3K4 mono and di-methylation at enhancers during embryonic stem cell, adipocyte and myogenic differentiation (Lee et al., 2013; Wang et al., 2016). Cranial intramembranous ossification is dependent on directed differentiation of a transient osteochondral progenitor cell towards either osteoblast or chondrocyte cell fate (Abzhanov et al., 2007; Akiyama et al., 2005; Bhatt et al., 2013). Osteochondral progenitors express both SOX9 and RUNX2, and the osteoblast or chondrocyte lineage decision will depend on expression levels of these transcription factors and whether SOX9 can effectively repress RUNX2 expression (Zhou et al., 2006). In a similar fashion, chondrocyte terminal differentiation is dependent on the SOX9 to RUNX2 balance. SOX9 is essential for chondrocyte proliferation (Akiyama et al., 2002). RUNX2 expression activates within these proliferating chondrocytes and promotes hypertrophic differentiation and endochondral ossification (Chen et al., 2014; Takarada et al., 2013). Continued SOX9 expression is required to keep RUNX2 expression under control to maintain a proliferative state and prevent hypertrophic chondrocyte and osteoblast differentiation (Dy et al., 2012). As we observe cranial NCC differentiation phenotypes in both intramembranous and endochondral ossification, KMT2D may be involved in regulating expression or activity of these transcription factors. Both KMT2D and UTX have described functions in regulating RUNX2 expression and activity during myoblast differentiation (Munehira et al., 2017; Rojas et al., 2015). We find that RUNX2 can be activated in KMT2D mutant NCCs (Figures 4E, 5F, 7M), so the methylase may act downstream to activate the RUNX2 transcriptional program. KMT2D also restricts chondrocyte differentiation within a teratocarcinoma cell line, through SHOX2 mediated SOX9 repression (Fahrner et al., 2019). In contrast to our findings, endochondral skeletal hypoplasia in *Kmt2d* heterozygous mice result from expanded growth plates with increased tibia chondrocyte hypertrophy (Fahrner et al., 2019). These differential findings could stem from KMT2D null as opposed to loss of function phenotypes or

cranial specific KMT2D functions that may differ from skeletal development. KMT2D knockdown in *Xenopus* embryos resulted in deficits in NCC neural plate specification and migration (Schwenty-Lara et al., 2019). While we do not observe a major defect in NCC migration, KMT2D may be partially redundant in mammalian NCC development with the KMT2C homolog as has been observed in other cell types (Hu et al., 2013; Lee et al., 2013). Knockout of both H3K4 methylases may produce severe developmental NCC abnormalities and more complete inhibition of chondrocyte or osteoblast differentiation.

Phenotypic heterogeneity within Kabuki syndrome has led to diagnostic difficulties and even misdiagnoses (Bramswig et al., 2015; Negri et al., 2019; Sakata et al., 2017; Schulz et al., 2014; Verhagen et al., 2014). Type 1 Kabuki syndrome (KS1) resulting from *KMT2D* mutation has the most consistent genotype to phenotype correlations whereby patients exhibit more typical facial dysmorphic features and palatal abnormalities (Adam et al., 2019; Banka et al., 2015; Makrythanasis et al., 2013; Miyake et al., 2013). Type 2 (KS2), *UTX* mutant Kabuki patients can exhibit varying severity with sexual dimorphism (Banka et al., 2015; Miyake et al., 2013). *UTX* hemizygous KS2 males had more severe motor delay and cognitive disability (Banka et al., 2015). This variable expressivity was even present in hereditary families whereby heterozygous *UTX* females carrying the same mutation as hemizygous *UTX* males lacked intellectual disability (Kim and Lee, 2017; Lederer et al., 2014). In these cases, heterozygous females have 1 functional copy of *UTX* while hemizygous males have the Y-chromosome homolog, *UTY*. The sexual dimorphism may be due to skewed X-chromosome inactivation in heterozygotes (Miyake et al., 2013) or lack of *UTY* function as a histone demethylase (Hong et al., 2007; Lan et al., 2007; Shpargel et al., 2012). However *UTX* function in mouse craniofacial development is redundant with *UTY* and does not require histone demethylase activity (Shpargel et al., 2017). Allelic heterogeneity also exists for KS1 as *KMT2D* missense mutations produced less severe facial phenotypes compared to truncating mutations (Miyake et al., 2013). Overall, the *UTX* causative facial dysmorphism in KS2 lacked some of the more typical Kabuki features that were more consistently present with loss of *KMT2D* function (Banka et al., 2015; Miyake et al., 2013). However, small cohort sizes, allelic heterogeneity, and sexual dimorphism have made cross comparisons difficult.

Modeling craniofacial development in the mouse with NCC specific knockout approaches has provided us with the opportunity to directly compare null knockout of *Kmt2d* to *Utx* to contrast regional specific function of the two chromatin factors (this study and Shpargel et al., 2017). Homozygous NCC knockout of both *Kmt2d* and *Utx* produced similar frontonasal hypoplasia. Both chromatin-modifying proteins affected osteochondral progenitor differentiation patterns in frontal primordia. In contrast, *Kmt2d* NCC knockout produced fully penetrant cleft palate, an observation that was only present in a small percentage of *Utx* knockout mice. Unlike *Utx*, *Kmt2d* NCC knockout produced more severe mandible hypoplasia, and micrognathia is a feature human Kabuki patients (Porntaveetus et al., 2018). Additionally, *Kmt2d* was uniquely required for cranial NCC dependent endochondral ossification events within the basicranium, mandibular condyle, and hyoid. Alterations to cranial base and condylar process growth can contribute to facial dysmorphology in craniofacial disorders (Lieberman et al., 2000; Neaux et al., 2018; Nie, 2005). We conclude that KMT2D does demonstrate region specific functions in NCC craniofacial development that may underlie phenotypic heterogeneity in KS1 and KS2 Kabuki patients. UTX either does not function in these cell types or has redundancy with other chromatin-modifying proteins. Notably, a homologous H3K27 demethylase, KDM6B (JMDJ3) functions in chondrocyte proliferation and hypertrophy in long bone endochondral ossification (Zhang et al., 2015a). Consistent with potential redundancy, we find that UTX and KDM6B expression overlaps in several NCC derived craniofacial tissues (Figure S2). In our future research, we will continue to examine the direct role of KMT2D towards induction of cranial NCC differentiation and explore cellular specific genomic redundancy between chromatin-modifying factors in this process.

Materials and Methods

Mice

All mouse experimental procedures were approved by the University of North Carolina Institutional Animal Care and Use Committee. Mouse strains were crossed for at least 4 generations onto C57BL/6J backgrounds. The *Kmt2d^{fl}* and *Utx^{fl}* alleles were previously described (Jang et al., 2019; Shpargel et al., 2014). The *Kdm6b^{GT}* allele (*Kdm6b^{tm1(KOMP)Wtsi}*), targeted in JM8 embryonic stem cells by the Knockout Mouse Project (KOMP), replaced *Kdm6b* exons 11-20 with a splicing trap and internal ribosome entry site for LacZ expression. ES cells were injected into *C57BL/6J-Tyr^{c-2J}* blastocysts to generate germline transmission. *Wnt1-Cre*, *Sox10-Cre*, and *Rosa^{Tomato}* reporter mice were imported from Jackson Labs (Danielian et al., 1998; Madisen et al., 2010; Matsuoka et al., 2005). The *Sox10-Cre* transgene was active in the male germline similar to the S4F:Cre line which utilizes a *Sox10* enhancer (Stine et al., 2009). Therefore, female mice carrying the *Sox10-Cre* allele were utilized for crossing into *Kmt2d*.

Histology and *in situ* hybridization

Embryonic fixation and sectioning was performed as described (Shpargel et al., 2012). For histology, samples were fixed in 4% paraformaldehyde overnight, embedded in paraffin, and sectioned (10 micron) on a microtome for hematoxylin and eosin (H&E) staining, picosirius red staining, or *in situ* hybridization. H&E staining was performed in Harris hematoxylin, blued with ammonium hydroxide, and counterstained with eosin. Picosirius red staining was performed with 0.1% Direct Red 80 (Sigma 365548-5G) dissolved in saturated picric acid. RNA *In situ* hybridization on sections was performed as described (Chandler et al., 2007) using T7 transcribed digoxigenin labeled riboprobes from regions indicated in the primers section. All probes were generated from unique regions with the *Kmt2d* probe based on a region utilized by the Allen Brain Atlas (<https://mouse.brain-map.org>) and the *Sox10* probe based on 3' regions from published reports (Kuhlbrodt et al., 1998; Southard-Smith et al., 1998). X-Gal staining was performed as described (Chandler et al., 2007).

Whole mount analyses

Whole mount skeletal preparations were fixed in 95% Ethanol and alizarin red and alcian blue staining was performed as described (Lufkin et al., 1992). Whole mount RNA *in situ* hybridization was performed as described (Chandler and Magnuson, 2016; Jacques-Fricke et al., 2012).

Immunofluorescence

For immunofluorescence, embryos were fixed for 1 hour in 4% paraformaldehyde, passed through sucrose gradient, and cryopreserved/frozen in sucrose/OCT prior to sectioning (10 micron) on a cryostat. Immunofluorescence was performed in PBS/3% BSA/10% goat serum/0.1% Triton X-100 using RUNX2 (1:800, Cell Signaling 12556S or 1:100, Abcam ab76956), COL2 (1:100, Thermo MA5-12789), OSX (1:150, Abcam ab22552), pH3S10 (1:500, Millipore 06-570), TMEM119 (1:150, Abcam ab209064), UTX (1:400, Cell Signaling 33510S), SOX9 (1:400, Millipore AB5535), BrdU (1:250, Abcam ab6326), and Cleaved Caspase 3 (1:400, Cell Signaling 9661S). BrdU labeling was performed by maternal intraperitoneal injection of 50 mg/kg BrdU (Sigma B5002-250MG) prepared in PBS 2 hours prior to embryonic dissection. BrdU labeled sections were treated in 2 N HCL/PBS for 30 minutes at 37 degrees before blocking. Sections were imaged with Zeiss axiovision software. Image stacks were deconvolved and z-projected. Measurements of bone lengths, differentiation domain lengths, and area were quantified with ImageJ (<https://imagej.nih.gov/ij/>).

Statistics

Statistical analysis for comparison between WT and *Kmt2d*^{CKO} samples were performed using a two-tailed Student's t-Test to determine significant differences between groups (p-value<0.05). Asterisks denote significant differences compared to WT (* = p-value < 0.05, ** = p-value < 0.01, *** = p-value < 0.001)

MEFs and western blotting

E9.5 MEFs were generated as described (Shpargel et al., 2012). For western blotting, nuclear lysates were prepared according to Invitrogen's nuclear extraction protocol. Western blotting was performed as described (Shpargel et al., 2012) with

anti-KMT2D (1:1000, generated in (Lee et al., 2013)) and anti-Nucleolin (1:5000, Bethyl Labs A300-711A).

RNA-seq

E14.25 palatal shelves were micro-dissected, and RNA was isolated with Trizol as directed (Thermo-Fisher) from 3 biological replicates of WT or *Kmt2d*^{ckO} embryos for cDNA synthesis, ligation of Truseq adapters, and library amplification (Kappa KK8580 mRNA HyperPrep Kit). Library samples were multiplexed for Nextseq 500 high output 25bp paired end sequencing. The quality of the sequence reads was evaluated with FastQC (<http://www.bioinformatics.babraham.ac.uk/projects/fastqc/>). Reads were mapped to the MM9 B6 genome using Tophat2 (Kim et al., 2013). We removed any sequencing data on the X and Y-chromosomes due to sex differences male and female embryos. Genic RNA-seq reads were counted with htseq-count (Anders et al., 2015) and analyzed by edgeR using DESeq2's independent filtering method to determine the cutoff for the minimum read counts per sample to identify significant (FDR < 0.05) differential expression (Anders and Huber, 2010; Robinson et al., 2010). KMT2D dependent gene expression was refined for genes that have higher levels of WT palate expression (RPKM > 2) with more dramatic *Kmt2d*^{ckO} expression changes (logFC < -1). Ingenuity Pathway Analysis and the Molecular Signatures Database (MSigDB) were utilized to analyze mis-expressed pathways based on RNA-seq expression data (<http://www.ingenuity.com/products/ipa>, <http://software.broadinstitute.org/gsea/msigdb/index.jsp>). RNA-seq datasets were submitted to GEO (GSE149688). RNA-seq was verified by qRT-PCR (Bio-Rad SsoFast EvaGreen, CFX96 real time system). All RT-PCR was normalized to *Gapdh* expression and graphed relative to control samples.

Primers

All genotyping and qRT-PCR primers are available upon request. Regions amplified by RT-PCR for subcloning, in vitro transcription, and in situ hybridization are as follows with T7 promoter underlined.

T7-Kmt2d-R: TAATACGACTCACTATAGGGCCCTTGCCAAAGAAAGTATCTG

Kmt2d-F: AAATAACACAGGGTCACAGCCT

T7-Sox10-R: TAATACGACTCACTATAGGGCCAGAAGCATTGATTTTATTACTTGG

Sox10-F: CTGAATGTGGGAAGTGGTCTG

T7-Col8a2-R: TAATACGACTCACTATAGGGTCCCATCCAAACCTGGTTTG

Col8a2-F: CTCTACCGATGCTGCCAATG

T7-Pcolce-R: TAATACGACTCACTATAGGGACATCAGGCAGCTGTCCTAG

Pcolce-F: TCTCTTCTGAAGGGAACGAG

Competing interests

No competing interests declared

Funding

This work was financially supported by a University of North Carolina Junior Faculty Development Award (KBS), a National Institutes of Health R01 award (R01GM101974, TM), and a National Institutes of Health R03 award (R03DE027101, KBS).

Data Availability

RNA-seq datasets were submitted to the Gene Expression Omnibus (GEO, GSE149688).

References

- Abzhanov, A., Rodda, S. J., McMahon, A. P. and Tabin, C. J.** (2007). Regulation of skeletogenic differentiation in cranial dermal bone. *Dev. Camb. Engl.* **134**, 3133–3144.
- Adam, M. P., Hudgins, L. and Hannibal, M.** (1993). Kabuki Syndrome. In *GeneReviews(R)* (ed. Pagon, R. A.), Adam, M. P.), Ardinger, H. H.), Wallace, S. E.), Amemiya, A.), Bean, L. J. H.), Bird, T. D.), Fong, C. T.), Mefford, H. C.), Smith, R. J. H.), et al.), p. Seattle (WA).
- Adam, M. P., Banka, S., Bjornsson, H. T., Bodamer, O., Chudley, A. E., Harris, J., Kawame, H., Lanpher, B. C., Lindsley, A. W., Merla, G., et al.** (2019). Kabuki syndrome: international consensus diagnostic criteria. *J. Med. Genet.* **56**, 89–95.
- Akiyama, H., Chaboissier, M.-C., Martin, J. F., Schedl, A. and de Crombrughe, B.** (2002). The transcription factor Sox9 has essential roles in successive steps of the chondrocyte differentiation pathway and is required for expression of Sox5 and Sox6. *Genes Dev.* **16**, 2813–2828.
- Akiyama, H., Kim, J.-E., Nakashima, K., Balmes, G., Iwai, N., Deng, J. M., Zhang, Z., Martin, J. F., Behringer, R. R., Nakamura, T., et al.** (2005). Osteochondroprogenitor cells are derived from Sox9 expressing precursors. *Proc. Natl. Acad. Sci. U. S. A.* **102**, 14665–14670.
- Anders, S. and Huber, W.** (2010). Differential expression analysis for sequence count data. *Genome Biol.* **11**, R106.
- Anders, S., Pyl, P. T. and Huber, W.** (2015). HTSeq--a Python framework to work with high-throughput sequencing data. *Bioinforma. Oxf. Engl.* **31**, 166–9.
- Ang, S. Y., Uebersohn, A., Spencer, C. I., Huang, Y., Lee, J. E., Ge, K. and Bruneau, B. G.** (2016). KMT2D regulates specific programs in heart development via histone H3 lysine 4 di-methylation. *Development* **143**, 810–21.
- Bajpai, R., Chen, D. A., Rada-Iglesias, A., Zhang, J., Xiong, Y., Helms, J., Chang, C. P., Zhao, Y., Swigut, T. and Wysocka, J.** (2010). CHD7 cooperates with PBAF to control multipotent neural crest formation. *Nature* **463**, 958–62.
- Banka, S., Lederer, D., Benoit, V., Jenkins, E., Howard, E., Bunstone, S., Kerr, B., McKee, S., Lloyd, I. C., Shears, D., et al.** (2015). Novel KDM6A (UTX) mutations and a clinical and molecular review of the X-linked Kabuki syndrome (KS2). *Clin Genet* **87**, 252–8.
- Berdasco, M. and Esteller, M.** (2013). Genetic syndromes caused by mutations in epigenetic genes. *Hum. Genet.* **132**, 359–383.
- Bhatt, S., Diaz, R. and Trainor, P. A.** (2013). Signals and switches in Mammalian neural crest cell differentiation. *Cold Spring Harb Perspect Biol* **5**.

- Bjornsson, H. T., Benjamin, J. S., Zhang, L., Weissman, J., Gerber, E. E., Chen, Y. C., Vaurio, R. G., Potter, M. C., Hansen, K. D. and Dietz, H. C.** (2014). Histone deacetylase inhibition rescues structural and functional brain deficits in a mouse model of Kabuki syndrome. *Sci Transl Med* **6**, 256ra135.
- Bögershausen, N., Tsai, I.-C., Pohl, E., Kiper, P. Ö. S., Beleggia, F., Percin, E. F., Keupp, K., Matchan, A., Milz, E., Alanay, Y., et al.** (2015). RAP1-mediated MEK/ERK pathway defects in Kabuki syndrome. *J. Clin. Invest.* **125**, 3585–3599.
- Bogershausen, N., Gatinois, V., Riehmer, V., Kayserili, H., Becker, J., Thoenes, M., Simsek-Kiper, P. O., Barat-Houari, M., Elcioglu, N. H., Wieczorek, D., et al.** (2016). Mutation Update for Kabuki Syndrome Genes KMT2D and KDM6A and Further Delineation of X-Linked Kabuki Syndrome Subtype 2. *Hum Mutat* **37**, 847–64.
- Bramswig, N. C., Lüdecke, H.-J., Alanay, Y., Albrecht, B., Barthelmie, A., Boduroglu, K., Braunholz, D., Caliebe, A., Chrzanowska, K. H., Czeschik, J. C., et al.** (2015). Exome sequencing unravels unexpected differential diagnoses in individuals with the tentative diagnosis of Coffin-Siris and Nicolaides-Baraitser syndromes. *Hum. Genet.* **134**, 553–568.
- Bush, J. O. and Jiang, R.** (2012). Palatogenesis: morphogenetic and molecular mechanisms of secondary palate development. *Dev. Camb. Engl.* **139**, 231–243.
- Carosso, G. A., Boukas, L., Augustin, J. J., Nguyen, H. N., Winer, B. L., Cannon, G. H., Robertson, J. D., Zhang, L., Hansen, K. D., Goff, L. A., et al.** (2019). Precocious neuronal differentiation and disrupted oxygen responses in Kabuki syndrome. *JCI Insight*.
- Chandler, R. L. and Magnuson, T.** (2016). The SWI/SNF BAF-A complex is essential for neural crest development. *Dev Biol* **411**, 15–24.
- Chandler, R. L., Chandler, K. J., McFarland, K. A. and Mortlock, D. P.** (2007). Bmp2 transcription in osteoblast progenitors is regulated by a distant 3' enhancer located 156.3 kilobases from the promoter. *Mol Cell Biol* **27**, 2934–51.
- Chen, H., Ghorji-Javed, F. Y., Rashid, H., Adhami, M. D., Serra, R., Gutierrez, S. E. and Javed, A.** (2014). Runx2 regulates endochondral ossification through control of chondrocyte proliferation and differentiation. *J. Bone Miner. Res. Off. J. Am. Soc. Bone Miner. Res.* **29**, 2653–2665.
- Chiquet, M., Blumer, S., Angelini, M., Mitsiadis, T. A. and Katsaros, C.** (2016). Mesenchymal Remodeling during Palatal Shelf Elevation Revealed by Extracellular Matrix and F-Actin Expression Patterns. *Front. Physiol.* **7**, 392.
- Cho, Y. W., Hong, T., Hong, S., Guo, H., Yu, H., Kim, D., Guszczynski, T., Dressler, G. R., Copeland, T. D., Kalkum, M., et al.** (2007). PTIP associates with MLL3- and MLL4-containing histone H3 lysine 4 methyltransferase complex. *J Biol Chem* **282**, 20395–406.

- Cocciadiferro, D., Augello, B., De Nittis, P., Zhang, J., Mandriani, B., Malerba, N., Squeo, G. M., Romano, A., Piccinni, B., Verri, T., et al.** (2018). Dissecting KMT2D missense mutations in Kabuki syndrome patients. *Hum. Mol. Genet.* **27**, 3651–3668.
- d'Amaro, R., Scheidegger, R., Blumer, S., Pazera, P., Katsaros, C., Graf, D. and Chiquet, M.** (2012). Putative functions of extracellular matrix glycoproteins in secondary palate morphogenesis. *Front. Physiol.* **3**, 377.
- Danielian, P. S., Muccino, D., Rowitch, D. H., Michael, S. K. and McMahon, A. P.** (1998). Modification of gene activity in mouse embryos in utero by a tamoxifen-inducible form of Cre recombinase. *Curr Biol* **8**, 1323–6.
- Dupin, E., Creuzet, S. and Le Douarin, N. M.** (2006). The contribution of the neural crest to the vertebrate body. *Adv Exp Med Biol* **589**, 96–119.
- Dy, P., Wang, W., Bhattaram, P., Wang, Q., Wang, L., Ballock, R. T. and Lefebvre, V.** (2012). Sox9 directs hypertrophic maturation and blocks osteoblast differentiation of growth plate chondrocytes. *Dev. Cell* **22**, 597–609.
- Fahrner, J. A., Lin, W.-Y., Riddle, R. C., Boukas, L., DeLeon, V. B., Chopra, S., Lad, S. E., Luperchio, T. R., Hansen, K. D. and Bjornsson, H. T.** (2019). Precocious chondrocyte differentiation disrupts skeletal growth in Kabuki syndrome mice. *JCI Insight* **4**,.
- Ferguson, J. W. and Atit, R. P.** (2019). A tale of two cities: The genetic mechanisms governing calvarial bone development. *Genes. N. Y. N 2000* **57**, e23248.
- Fu, X., Xu, J., Chaturvedi, P., Liu, H., Jiang, R. and Lan, Y.** (2017). Identification of Osr2 Transcriptional Target Genes in Palate Development. *J Dent Res* **96**, 1451–1458.
- Goodnough, L. H., Chang, A. T., Treloar, C., Yang, J., Scacheri, P. C. and Atit, R. P.** (2012). Twist1 mediates repression of chondrogenesis by β -catenin to promote cranial bone progenitor specification. *Dev. Camb. Engl.* **139**, 4428–4438.
- Hannibal, M. C., Buckingham, K. J., Ng, S. B., Ming, J. E., Beck, A. E., McMillin, M. J., Gildersleeve, H. I., Bigham, A. W., Tabor, H. K., Mefford, H. C., et al.** (2011). Spectrum of MLL2 (ALR) mutations in 110 cases of Kabuki syndrome. *Am. J. Med. Genet. A.* **155A**, 1511–1516.
- Hari, L., Miescher, I., Shakhova, O., Suter, U., Chin, L., Taketo, M., Richardson, W. D., Kessaris, N. and Sommer, L.** (2012). Temporal control of neural crest lineage generation by Wnt/ β -catenin signaling. *Dev. Camb. Engl.* **139**, 2107–2117.
- Hisa, I., Inoue, Y., Hendy, G. N., Canaff, L., Kitazawa, R., Kitazawa, S., Komori, T., Sugimoto, T., Seino, S. and Kaji, H.** (2011). Parathyroid Hormone-responsive Smad3-related Factor, Tmem119, Promotes Osteoblast Differentiation and Interacts with the Bone Morphogenetic Protein-Runx2 Pathway. *J. Biol. Chem.* **286**, 9787–9796.

- Hong, S., Cho, Y. W., Yu, L. R., Yu, H., Veenstra, T. D. and Ge, K.** (2007). Identification of JmjC domain-containing UTX and JMJD3 as histone H3 lysine 27 demethylases. *Proc Natl Acad Sci U A* **104**, 18439–44.
- Hu, D., Gao, X., Morgan, M. A., Herz, H. M., Smith, E. R. and Shilatifard, A.** (2013). The MLL3/MLL4 branches of the COMPASS family function as major histone H3K4 monomethylases at enhancers. *Mol Cell Biol* **33**, 4745–54.
- Hu, N., Strobl-Mazzulla, P. H. and Bronner, M. E.** (2014). Epigenetic regulation in neural crest development. *Dev. Biol.* **396**, 159–168.
- Ishii, M., Merrill, A. E., Chan, Y.-S., Gitelman, I., Rice, D. P. C., Sucov, H. M. and Maxson, R. E.** (2003). Msx2 and Twist cooperatively control the development of the neural crest-derived skeletogenic mesenchyme of the murine skull vault. *Dev. Camb. Engl.* **130**, 6131–6142.
- Jacques-Fricke, B. T., Roffers-Agarwal, J. and Gammill, L. S.** (2012). DNA methyltransferase 3b is dispensable for mouse neural crest development. *PLoS One* **7**, e47794.
- Jang, Y., Broun, A., Wang, C., Park, Y. K., Zhuang, L., Lee, J. E., Froimchuk, E., Liu, C. and Ge, K.** (2019). H3.3K4M destabilizes enhancer H3K4 methyltransferases MLL3/MLL4 and impairs adipose tissue development. *Nucleic Acids Res* **47**, 607–620.
- Jiang, X., Iseki, S., Maxson, R. E., Sucov, H. M. and Morriss-Kay, G. M.** (2002). Tissue origins and interactions in the mammalian skull vault. *Dev Biol* **241**, 106–16.
- Jin, J.-Z., Tan, M., Warner, D. R., Darling, D. S., Higashi, Y., Gridley, T. and Ding, J.** (2010). Mesenchymal cell re-modeling during mouse secondary palate re-orientation. *Dev. Dyn. Off. Publ. Am. Assoc. Anat.* **239**, 2110–2117.
- Kim, J. and Lee, C. G.** (2017). Coinheritance of Novel Mutations in SCN1A Causing GEFS+ and in KDM6A Causing Kabuki Syndrome in a Family. *Ann Clin Lab Sci* **47**, 229–235.
- Kim, D., Pertea, G., Trapnell, C., Pimentel, H., Kelley, R. and Salzberg, S. L.** (2013). TopHat2: accurate alignment of transcriptomes in the presence of insertions, deletions and gene fusions. *Genome Biol* **14**, R36.
- Kuhlbrodt, K., Herbarth, B., Sock, E., Hermans-Borgmeyer, I. and Wegner, M.** (1998). Sox10, a novel transcriptional modulator in glial cells. *J. Neurosci. Off. J. Soc. Neurosci.* **18**, 237–250.
- Kuroki, Y., Suzuki, Y., Chyo, H., Hata, A. and Matsui, I.** (1981). A new malformation syndrome of long palpebral fissures, large ears, depressed nasal tip, and skeletal anomalies associated with postnatal dwarfism and mental retardation. *J. Pediatr.* **99**, 570–573.

- Lan, F., Bayliss, P. E., Rinn, J. L., Whetstone, J. R., Wang, J. K., Chen, S., Iwase, S., Alpatov, R., Issaeva, I., Canaani, E., et al. (2007). A histone H3 lysine 27 demethylase regulates animal posterior development. *Nature* **449**, 689–94.
- Lederer, D., Grisart, B., Digilio, M. C., Benoit, V., Crespin, M., Ghariani, S. C., Maystadt, I., Dallapiccola, B. and Verellen-Dumoulin, C. (2012). Deletion of KDM6A, a histone demethylase interacting with MLL2, in three patients with Kabuki syndrome. *Am J Hum Genet* **90**, 119–24.
- Lederer, D., Shears, D., Benoit, V., Verellen-Dumoulin, C. and Maystadt, I. (2014). A three generation X-linked family with Kabuki syndrome phenotype and a frameshift mutation in KDM6A. *Am J Med Genet A* **164A**, 1289–92.
- Lee, J. E., Wang, C., Xu, S., Cho, Y. W., Wang, L., Feng, X., Baldridge, A., Sartorelli, V., Zhuang, L., Peng, W., et al. (2013). H3K4 mono- and di-methyltransferase MLL4 is required for enhancer activation during cell differentiation. *Elife* **2**, e01503.
- Li, W., Xiong, Y., Shang, C., Twu, K. Y., Hang, C. T., Yang, J., Han, P., Lin, C. Y., Lin, C. J., Tsai, F. C., et al. (2013). Brg1 governs distinct pathways to direct multiple aspects of mammalian neural crest cell development. *Proc Natl Acad Sci U S A* **110**, 1738–43.
- Lieberman, D. E., Pearson, O. M. and Mowbray, K. M. (2000). Basicranial influence on overall cranial shape. *J. Hum. Evol.* **38**, 291–315.
- Lintas, C. and Persico, A. M. (2018). Unraveling molecular pathways shared by Kabuki and Kabuki-like syndromes. *Clin. Genet.* **94**, 283–295.
- Logan, S. M., Ruest, L.-B., Benson, M. D. and Svoboda, K. K. H. (2019). Extracellular Matrix in Secondary Palate Development. *Anat. Rec. Hoboken NJ* 2007.
- Lufkin, T., Mark, M., Hart, C. P., Dolle, P., LeMeur, M. and Chambon, P. (1992). Homeotic transformation of the occipital bones of the skull by ectopic expression of a homeobox gene. *Nature* **359**, 835–41.
- Madisen, L., Zwingman, T. A., Sunkin, S. M., Oh, S. W., Zariwala, H. A., Gu, H., Ng, L. L., Palmiter, R. D., Hawrylycz, M. J., Jones, A. R., et al. (2010). A robust and high-throughput Cre reporting and characterization system for the whole mouse brain. *Nat Neurosci* **13**, 133–40.
- Makrythanasis, P., van Bon, B. W., Steehouwer, M., Rodríguez-Santiago, B., Simpson, M., Dias, P., Anderlid, B. M., Arts, P., Bhat, M., Augello, B., et al. (2013). MLL2 mutation detection in 86 patients with Kabuki syndrome: a genotype-phenotype study. *Clin. Genet.* **84**, 539–545.
- Matsuoka, T., Ahlberg, P. E., Kessar, N., Iannarelli, P., Dennehy, U., Richardson, W. D., McMahon, A. P. and Koentges, G. (2005). Neural crest origins of the neck and shoulder. *Nature* **436**, 347–355.

- McBratney-Owen, B., Iseki, S., Bamforth, S. D., Olsen, B. R. and Morriss-Kay, G. M.** (2008). Development and tissue origins of the mammalian cranial base. *Dev Biol* **322**, 121–32.
- Micale, L., Augello, B., Fusco, C., Selicorni, A., Loviglio, M. N., Silengo, M. C., Reymond, A., Gumiero, B., Zucchetti, F., D’Addetta, E. V., et al.** (2011). Mutation spectrum of MLL2 in a cohort of Kabuki syndrome patients. *Orphanet J. Rare Dis.* **6**, 38.
- Minoux, M., Holwerda, S., Vitobello, A., Kitazawa, T., Kohler, H., Stadler, M. B. and Rijli, F. M.** (2017). Gene bivalency at Polycomb domains regulates cranial neural crest positional identity. *Science* **355**,.
- Miyake, N., Koshimizu, E., Okamoto, N., Mizuno, S., Ogata, T., Nagai, T., Kosho, T., Ohashi, H., Kato, M., Sasaki, G., et al.** (2013). MLL2 and KDM6A mutations in patients with Kabuki syndrome. *Am J Med Genet A* **161A**, 2234–43.
- Munehira, Y., Yang, Z. and Gozani, O.** (2017). Systematic Analysis of Known and Candidate Lysine Demethylases in the Regulation of Myoblast Differentiation. *J. Mol. Biol.* **429**, 2055–2065.
- Nakashima, K., Zhou, X., Kunkel, G., Zhang, Z., Deng, J. M., Behringer, R. R. and de Crombrughe, B.** (2002). The novel zinc finger-containing transcription factor osterix is required for osteoblast differentiation and bone formation. *Cell* **108**, 17–29.
- Neaux, D., Sansalone, G., Ledogar, J. A., Heins Ledogar, S., Luk, T. H. Y. and Wroe, S.** (2018). Basicranium and face: Assessing the impact of morphological integration on primate evolution. *J. Hum. Evol.* **118**, 43–55.
- Negri, G., Magini, P., Milani, D., Crippa, M., Biamino, E., Piccione, M., Sotgiu, S., Perrià, C., Vitiello, G., Frontali, M., et al.** (2019). Exploring by whole exome sequencing patients with initial diagnosis of Rubinstein-Taybi syndrome: the interconnections of epigenetic machinery disorders. *Hum. Genet.* **138**, 257–269.
- Ng, S. B., Bigham, A. W., Buckingham, K. J., Hannibal, M. C., McMillin, M. J., Gildersleeve, H. I., Beck, A. E., Tabor, H. K., Cooper, G. M., Mefford, H. C., et al.** (2010). Exome sequencing identifies MLL2 mutations as a cause of Kabuki syndrome. *Nat Genet* **42**, 790–3.
- Nie, X.** (2005). Cranial base in craniofacial development: developmental features, influence on facial growth, anomaly, and molecular basis. *Acta Odontol. Scand.* **63**, 127–135.
- Niikawa, N., Matsuura, N., Fukushima, Y., Ohsawa, T. and Kajii, T.** (1981). Kabuki make-up syndrome: a syndrome of mental retardation, unusual facies, large and protruding ears, and postnatal growth deficiency. *J Pediatr* **99**, 565–9.
- Niikawa, N., Kuroki, Y., Kajii, T., Matsuura, N., Ishikiriya, S., Tonoki, H., Ishikawa, N., Yamada, Y., Fujita, M., Umemoto, H., et al.** (1988). Kabuki make-

up (Niikawa-Kuroki) syndrome: a study of 62 patients. *Am J Med Genet* **31**, 565–89.

Petrij, F., Giles, R. H., Dauwerse, H. G., Saris, J. J., Hennekam, R. C., Masuno, M., Tommerup, N., van Ommen, G. J., Goodman, R. H., Peters, D. J., et al. (1995). Rubinstein-Taybi syndrome caused by mutations in the transcriptional co-activator CBP. *Nature* **376**, 348–51.

Porntaveetus, T., Abid, M. F., Theerapanon, T., Srichomthong, C., Ohazama, A., Kawasaki, K., Kawasaki, M., Suphapeetiporn, K., Sharpe, P. T. and Shotelersuk, V. (2018). Expanding the Oro-Dental and Mutational Spectra of Kabuki Syndrome and Expression of KMT2D and KDM6A in Human Tooth Germs. *Int J Biol Sci* **14**, 381–389.

Rada-Iglesias, A., Bajpai, R., Prescott, S., Brugmann, S. A., Swigut, T. and Wysocka, J. (2012). Epigenomic annotation of enhancers predicts transcriptional regulators of human neural crest. *Cell Stem Cell* **11**, 633–48.

Robinson, M. D., McCarthy, D. J. and Smyth, G. K. (2010). edgeR: a Bioconductor package for differential expression analysis of digital gene expression data. *Bioinforma. Oxf. Engl.* **26**, 139–40.

Roelfsema, J. H., White, S. J., Ariyurek, Y., Bartholdi, D., Niedrist, D., Papadia, F., Bacino, C. A., den Dunnen, J. T., van Ommen, G. J., Breuning, M. H., et al. (2005). Genetic heterogeneity in Rubinstein-Taybi syndrome: mutations in both the CBP and EP300 genes cause disease. *Am J Hum Genet* **76**, 572–80.

Rojas, A., Aguilar, R., Henriquez, B., Lian, J. B., Stein, J. L., Stein, G. S., van Wijnen, A. J., van Zundert, B., Allende, M. L. and Montecino, M. (2015). Epigenetic Control of the Bone-master Runx2 Gene during Osteoblast-lineage Commitment by the Histone Demethylase JARID1B/KDM5B. *J. Biol. Chem.* **290**, 28329–28342.

Sakata, S., Okada, S., Aoyama, K., Hara, K., Tani, C., Kagawa, R., Utsunomiya-Nakamura, A., Miyagawa, S., Ogata, T., Mizuno, H., et al. (2017). Individual Clinically Diagnosed with CHARGE Syndrome but with a Mutation in KMT2D, a Gene Associated with Kabuki Syndrome: A Case Report. *Front. Genet.* **8**, 210.

Sanka, M., Tangsinmankong, N., Loscalzo, M., Sleasman, J. W. and Dorsey, M. J. (2007). Complete DiGeorge syndrome associated with CHD7 mutation. *J Allergy Clin Immunol* **120**, 952–4.

Santagati, F. and Rijli, F. M. (2003). Cranial neural crest and the building of the vertebrate head. *Nat Rev Neurosci* **4**, 806–18.

Santen, G. W., Aten, E., Sun, Y., Almomani, R., Gilissen, C., Nielsen, M., Kant, S. G., Snoeck, I. N., Peeters, E. A., Hilhorst-Hofstee, Y., et al. (2012). Mutations in SWI/SNF chromatin remodeling complex gene ARID1B cause Coffin-Siris syndrome. *Nat Genet* **44**, 379–80.

- Schulz, Y., Freese, L., Manz, J., Zoll, B., Volter, C., Brockmann, K., Bogershausen, N., Becker, J., Wollnik, B. and Pauli, S. (2014). CHARGE and Kabuki syndromes: a phenotypic and molecular link. *Hum Mol Genet* **23**, 4396–405.
- Schwenty-Lara, J., Nehl, D. and Borchers, A. (2019). The histone methyltransferase KMT2D, mutated in Kabuki syndrome patients, is required for neural crest cell formation and migration. *Hum. Mol. Genet.*
- Serbedzija, G. N., Bronner-Fraser, M. and Fraser, S. E. (1992). Vital dye analysis of cranial neural crest cell migration in the mouse embryo. *Development* **116**, 297–307.
- Shpargel, K. B., Sengoku, T., Yokoyama, S. and Magnuson, T. (2012). UTX and UTY demonstrate histone demethylase-independent function in mouse embryonic development. *PLoS Genet* **8**, e1002964.
- Shpargel, K. B., Starmer, J., Yee, D., Pohlers, M. and Magnuson, T. (2014). KDM6 Demethylase Independent Loss of Histone H3 Lysine 27 Trimethylation during Early Embryonic Development. *PLoS Genet* **10**, e1004507.
- Shpargel, K. B., Starmer, J., Wang, C., Ge, K. and Magnuson, T. (2017). UTX-guided neural crest function underlies craniofacial features of Kabuki syndrome. *Proc. Natl. Acad. Sci. U. S. A.* **114**, E9046–E9055.
- Southard-Smith, E. M., Kos, L. and Pavan, W. J. (1998). Sox10 mutation disrupts neural crest development in Dom Hirschsprung mouse model. *Nat. Genet.* **18**, 60–64.
- Sperry, E. D., Hurd, E. A., Durham, M. A., Reamer, E. N., Stein, A. B. and Martin, D. M. (2014). The chromatin remodeling protein CHD7, mutated in CHARGE syndrome, is necessary for proper craniofacial and tracheal development. *Dev Dyn* **243**, 1055–66.
- Stine, Z. E., Huynh, J. L., Loftus, S. K., Gorkin, D. U., Salmasi, A. H., Novak, T., Purves, T., Miller, R. A., Antonellis, A., Gearhart, J. P., et al. (2009). Oligodendroglial and Pan-neural Crest Expression of Cre Recombinase Directed by Sox10 Enhancer. *Genes. N. Y. N 2000* **47**, 765–770.
- Strobl-Mazzulla, P. H., Marini, M. and Buzzi, A. (2012). Epigenetic landscape and miRNA involvement during neural crest development. *Dev. Dyn. Off. Publ. Am. Assoc. Anat.* **241**, 1849–1856.
- Szabo-Rogers, H. L., Smithers, L. E., Yakob, W. and Liu, K. J. (2010). New directions in craniofacial morphogenesis. *Dev. Biol.* **341**, 84–94.
- Takarada, T., Hinoi, E., Nakazato, R., Ochi, H., Xu, C., Tsuchikane, A., Takeda, S., Karsenty, G., Abe, T., Kiyonari, H., et al. (2013). An analysis of skeletal development in osteoblast-specific and chondrocyte-specific runt-related transcription factor-2 (Runx2) knockout mice. *J. Bone Miner. Res. Off. J. Am. Soc. Bone Miner. Res.* **28**, 2064–2069.

- Trainor, P. A.** (2005). Specification of neural crest cell formation and migration in mouse embryos. *Semin Cell Dev Biol* **16**, 683–93.
- Tsurusaki, Y., Okamoto, N., Ohashi, H., Kosho, T., Imai, Y., Hibi-Ko, Y., Kaname, T., Naritomi, K., Kawame, H., Wakui, K., et al.** (2012). Mutations affecting components of the SWI/SNF complex cause Coffin-Siris syndrome. *Nat Genet* **44**, 376–8.
- Van Laarhoven, P. M., Neitzel, L. R., Quintana, A. M., Geiger, E. A., Zackai, E. H., Clouthier, D. E., Artinger, K. B., Ming, J. E. and Shaikh, T. H.** (2015). Kabuki syndrome genes KMT2D and KDM6A: functional analyses demonstrate critical roles in craniofacial, heart and brain development. *Hum Mol Genet* **24**, 4443–53.
- Verhagen, J. M., Oostdijk, W., Terwisscha van Scheltinga, C. E., Schalijs-Delfos, N. E. and van Bever, Y.** (2014). An unusual presentation of Kabuki syndrome: clinical overlap with CHARGE syndrome. *Eur J Med Genet* **57**, 510–2.
- Visser, L. E., van Ravenswaaij, C. M., Admiraal, R., Hurst, J. A., de Vries, B. B., Janssen, I. M., van der Vliet, W. A., Huys, E. H., de Jong, P. J., Hamel, B. C., et al.** (2004). Mutations in a new member of the chromodomain gene family cause CHARGE syndrome. *Nat Genet* **36**, 955–7.
- Vivatbutsi, P., Ichinose, S., Hytönen, M., Sainio, K., Eto, K. and Iseki, S.** (2008). Impaired meningeal development in association with apical expansion of calvarial bone osteogenesis in the *Foxc1* mutant. *J. Anat.* **212**, 603–611.
- Wang, C., Lee, J. E., Lai, B., Macfarlan, T. S., Xu, S., Zhuang, L., Liu, C., Peng, W. and Ge, K.** (2016). Enhancer priming by H3K4 methyltransferase MLL4 controls cell fate transition. *Proc Natl Acad Sci U S A* **113**, 11871–11876.
- Wu, M., Li, J., Engleka, K. A., Zhou, B., Lu, M. M., Plotkin, J. B. and Epstein, J. A.** (2008). Persistent expression of Pax3 in the neural crest causes cleft palate and defective osteogenesis in mice. *J. Clin. Invest.* **118**, 2076–2087.
- Yoshida, T., Vivatbutsi, P., Morriss-Kay, G., Saga, Y. and Iseki, S.** (2008). Cell lineage in mammalian craniofacial mesenchyme. *Mech Dev* **125**, 797–808.

- Yu, K. and Ornitz, D. M.** (2011). Histomorphological study of palatal shelf elevation during murine secondary palate formation. *Dev. Dyn. Off. Publ. Am. Assoc. Anat.* **240**, 1737–1744.
- Zhang, F., Xu, L., Xu, L., Xu, Q., Li, D., Yang, Y., Karsenty, G. and Chen, C. D.** (2015a). JMJD3 promotes chondrocyte proliferation and hypertrophy during endochondral bone formation in mice. *J. Mol. Cell Biol.* **7**, 23–34.
- Zhang, J., Yang, R., Liu, Z., Hou, C., Zong, W., Zhang, A., Sun, X. and Gao, J.** (2015b). Loss of lysyl oxidase-like 3 causes cleft palate and spinal deformity in mice. *Hum. Mol. Genet.* **24**, 6174–6185.
- Zhou, G., Zheng, Q., Engin, F., Munivez, E., Chen, Y., Sebald, E., Krakow, D. and Lee, B.** (2006). Dominance of SOX9 function over RUNX2 during skeletogenesis. *Proc. Natl. Acad. Sci. U. S. A.* **103**, 19004–19009.

Figures

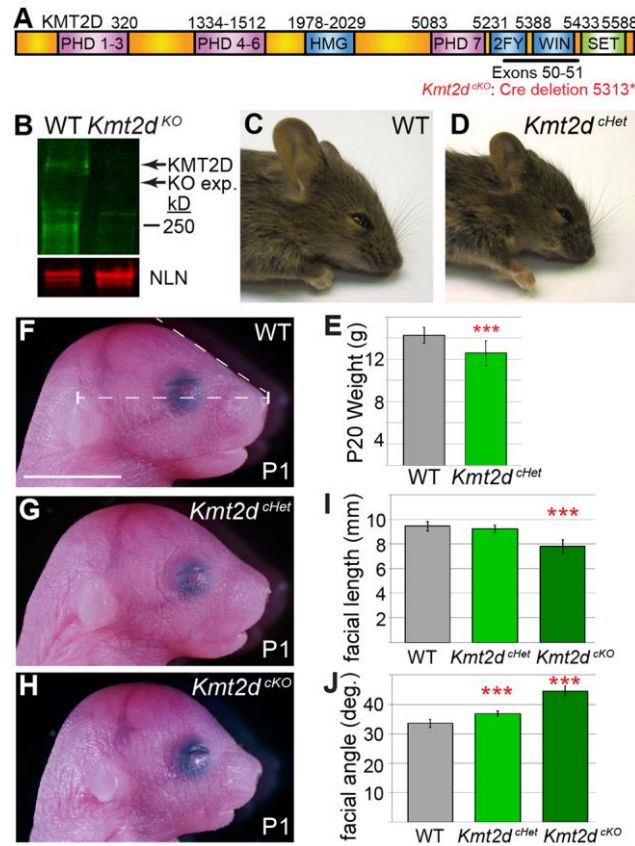


Figure 1: *Kmt2d* NCC mutant facial phenotypes. (A) Protein schematic of KMT2D whereby numbering indicates amino acid position. The *Kmt2d* conditional allele has loxP sites flanking exons 50-51. Cre deletion creates a nonsense frameshift deleting the SET methylase domain. PHD=plant homeodomain, HMG=high-mobility group, 2FY=2 FY rich domains, WIN=WDR5 interaction motif. (B) Western blot of WT or *Kmt2d* knockout MEFs for KMT2D protein (green) or Nucleolin (red) control. Illustrated is the expected size range for KO SET deletion (KO exp: 568 kD). (C-D) Images of WT and NCC heterozygous *Kmt2d*^{cHet} mice at weaning. (E) Quantitation of P20 *Kmt2d*^{cHet} weight. N ≥ 12. (F-H) P1 WT, *Kmt2d*^{cHet}, and *Kmt2d*^{cKO} facial phenotypes. Solid white scale bar in F = 5 mm. (I) Quantitation of P1 nasal tip to otic facial length as depicted by dashed line in part F. N ≥ 6. (J) Quantitation of P1 facial angle as depicted between dashed lines in part F. N ≥ 6.

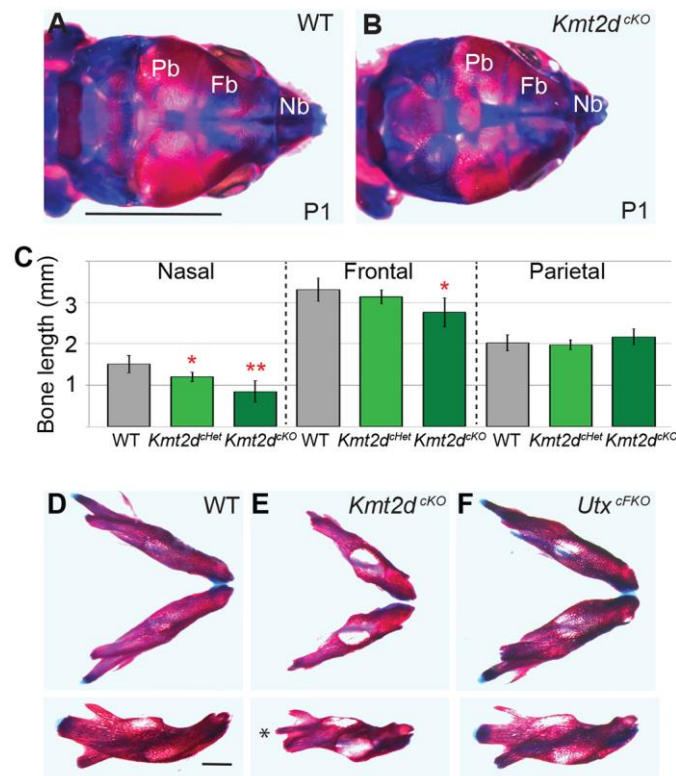


Figure 2: *Kmt2d* NCC mutant cranial skeletal structure. (A-B) Whole mount images of alizarin red/alcian blue staining of bone/cartilage at P1. Pb: parietal bone, Fb: frontal bone, Nb: nasal bone. Black scale bar in A = 5 mm. (C) Quantitation of *Kmt2d*^{chHt} and *Kmt2d*^{cKO} Nb, Fb, and Pb lengths. N ≥ 4. (D-F) Whole mount skeletal staining of dissected *Kmt2d*^{cKO} (E) and *Utx*^{cFKO} (F) mandibles with side view on the bottom. Asterisk in part E denotes loss of mandibular condylar cartilage and smaller condylar process in *Kmt2d*^{cKO}. Black scale bar in D = 1 mm.

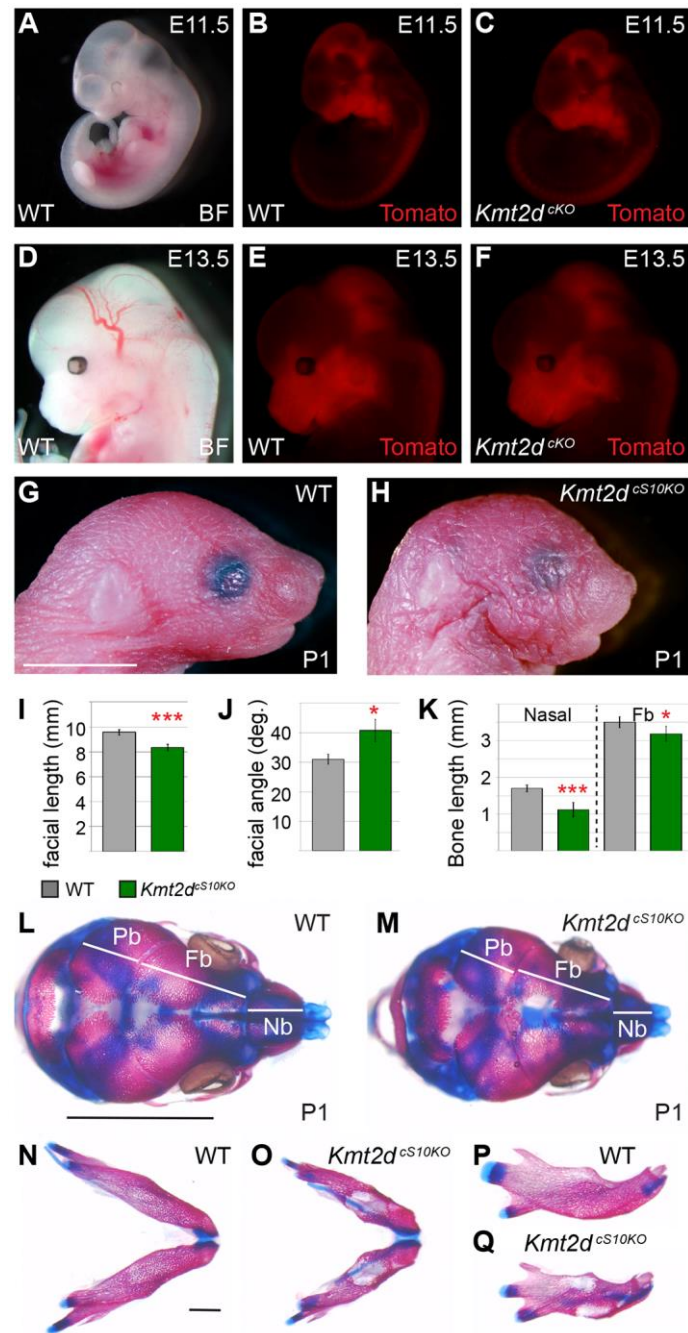


Figure 3: *Kmt2d* cranial NCC lineage tracing and *Sox10-Cre* knockout. (A-C) E11.5 brightfield (BF) and tomato fluorescent images of embryos carrying *Wnt1-Cre* and the *Rosa^{Tomato}* reporter. (D-F) BF and tomato fluorescent images of NCC lineage tracing in E13.5 *Wnt1-Cre* embryos. *Kmt2d^{ckO}* NCCs reside in similar cranial regions with similar fluorescent intensity. (G-H) P1 WT and *Kmt2d^{cS10KO}* facial phenotypes. Solid white scale bar in G = 5 mm. (I) Quantitation of P1 nasal tip to otic facial length as depicted by dashed line in Figure 1F. N ≥ 4. (J) Quantitation of P1 facial angle as

depicted between dashed lines in Figure 1F. $N \geq 4$. (K) Quantitation of WT and *Kmt2d*^{cS10KO} nasal and frontal bone (Fb) lengths depicted in parts L-M. $N \geq 4$. (L-M) Whole mount images of alizarin red/alcian blue staining of bone/cartilage at P1. Pb: parietal bone, Fb: frontal bone, Nb: nasal bone. Black scale bar in L = 5 mm. (N-Q) Whole mount skeletal staining of dissected WT and *Kmt2d*^{cS10KO} mandibles with side view (P-Q). Black scale bar in N = 1 mm.

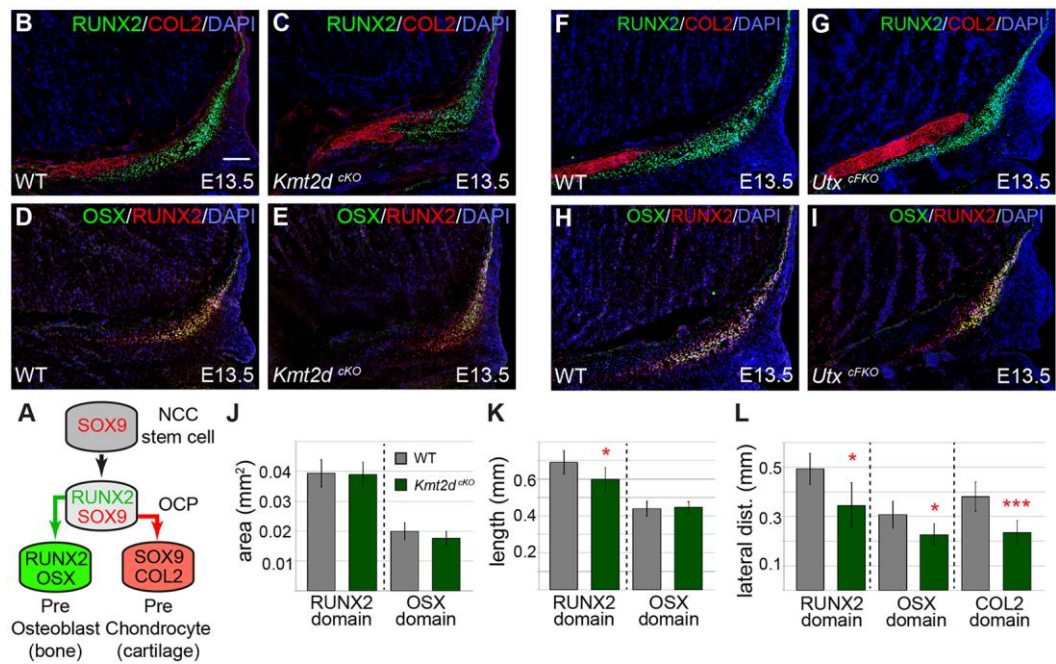


Figure 4: Analysis of osteochondral differentiation in *Kmt2d*^{cKO} frontal primordia. (A) Schematic of cranial NCC osteochondral differentiation with cellular markers. OCP: osteochondral progenitor cell. (B-E) E13.5 WT and *Kmt2d*^{cKO} NCC differentiation in coronal sections of supraorbital frontal primordia with immunofluorescence for markers of pre-osteoblasts (RUNX2 and OSX) or pre-chondrocytes (COL2). White scale bar in B = 0.1 mm. (F-I) E13.5 WT and *Utx*^{cFKO} NCC pre-osteoblasts and pre-chondrocyte differentiation in coronal frontal primordia sections. (J) Quantitation of the RUNX2+ area and OSX+ areas in sections corresponding to parts B-E. N = 6: 3 biological samples with left and right supraorbital measurements. (K) Quantitation of the lengths of RUNX2+ and OSX+ domains in sections corresponding to parts B-E. (L) Quantitation of the distance that RUNX2+ or OSX+ domains extend towards the interior of the head as measured from the most lateral edge of each domain. COL2 domains were measured to determine the interior distance at which this domain forms with respect to most lateral edge of the RUNX2 domain.

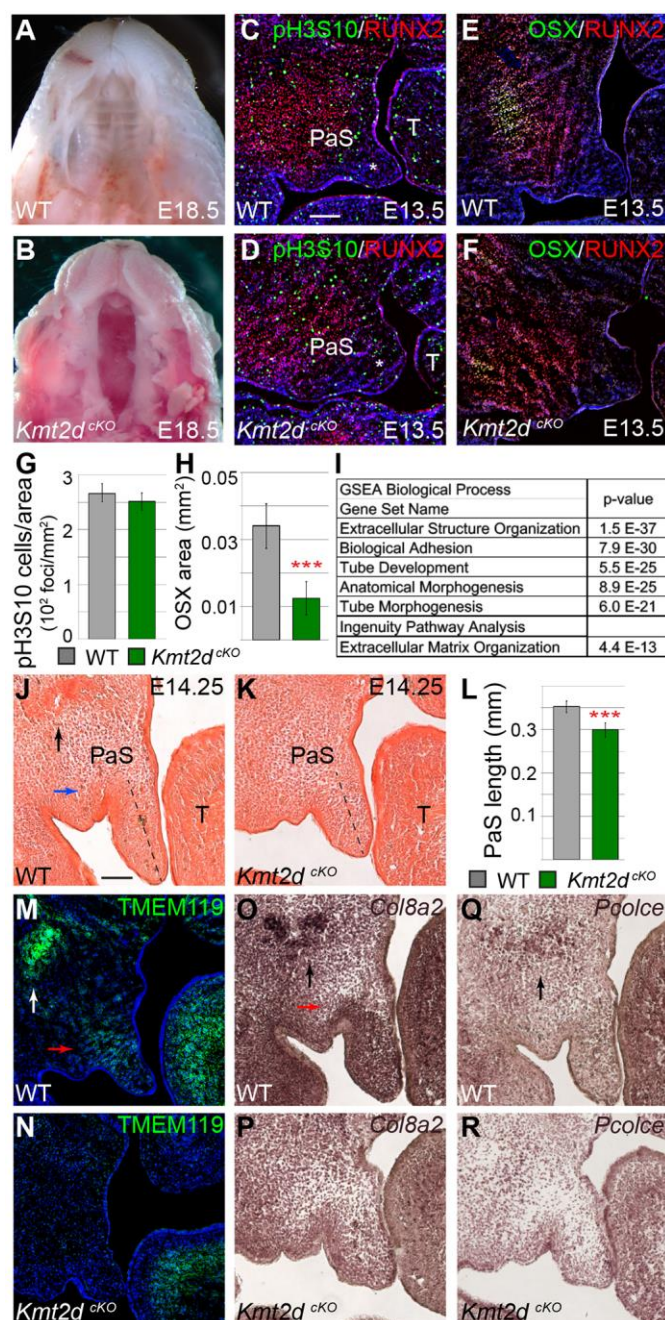


Figure 5: *Kmt2d*^{cKO} function in palatogenesis. (A-B) P1 WT or *Kmt2d*^{cKO} mandibles were dissected to illustrate fully penetrant *Kmt2d*^{cKO} cleft palate. (C-D) Coronal sections of WT or *Kmt2d*^{cKO} anterior regions of the E13.5 secondary palatal shelves with immunofluorescence for RUNX2 and pH3S10 overlaid with DAPI. PaS: palatal shelf, T: tongue. White scale bar in C = 0.1 mm. (E-F) WT or *Kmt2d*^{cKO} immunofluorescence for RUNX2 and OSX in E13.5 secondary palatal shelves overlaid with DAPI. (G) Quantitation of the number of cells in mitosis (pH3S10 foci)

per unit area. N = 12: 3 biological samples with left and right palatal shelf measurements from 2 anterior-central sections spaced 80 microns apart. (H) Quantitation of the area of RUNX2+ pre-osteoblasts that have condensed and differentiated (OSX+). (I) Gene Set Enrichment Analysis and Ingenuity Pathway Analysis for biological function based on RNA-seq identified *Kmt2d^{cko}* genes that have lost expression in E14.25 unfused palatal shelves. (J-K) Picrosirius red staining of E14.25 WT and *Kmt2d^{cko}* palatal coronal sections. Black arrow highlights the osteoblast differentiation domain and the blue arrow points to enrichment in subepithelial mesenchyme. Dashed line indicates region measured in part L. Black scale bar in J = 0.1 mm. (L) Measured length of the *Kmt2d^{cko}* distal palate tip indicated in parts J-K. N = 3 sets of palatal shelf distal tip measurements averaged from 2 anterior-central sections spaced 80 microns apart. (M-N) TMEM119 immunofluorescence in E14.25 coronal palate sections. White arrow highlights osteoblasts and red arrow depicts enrichment in distal palatal shelf mesenchyme. N = 4 sets of palatal shelves analyzed. (O-R) E14.25 RNA *in situ* hybridization for *Col8a2* (O-P) or *Pcolce* (Q-R) with osteoblast (black arrows) and subepithelial mesenchyme (red arrow) indicating regional expression reduced in *Kmt2d^{cko}*. N = 3 sets of palatal shelves analyzed.

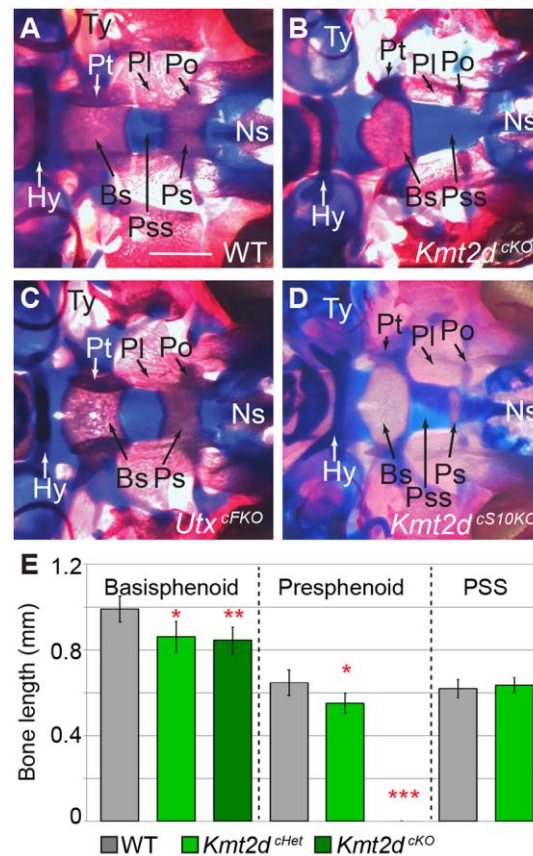


Figure 6: *Kmt2d^{cKO}* function in cranial base structure. (A-C) Higher magnification, ventral view of WT (A), *Kmt2d^{cKO}* (B), *Utx^{cFKO}* (C), or *Kmt2d^{cS10KO}* (D) cranial base region of whole mount alizarin red/alcian blue skeletal staining of bone/cartilage at P1. Bs: basisphenoid, Ps: presphenoid, Pss: presphenoidal synchondrosis, Pt: pterygoid, Pl: palatine, Po: postoptic roots of the sphenoid, Ns: nasal septum, Hy: hyoid, Ty: tympanic. White scale bar in A = 1 mm. (E) Quantitation of midline lengths for basisphenoid bone, presphenoid bone, and presphenoidal synchondrosis from whole mount alizarin red/alcian blue skeletal staining. N ≥ 4.

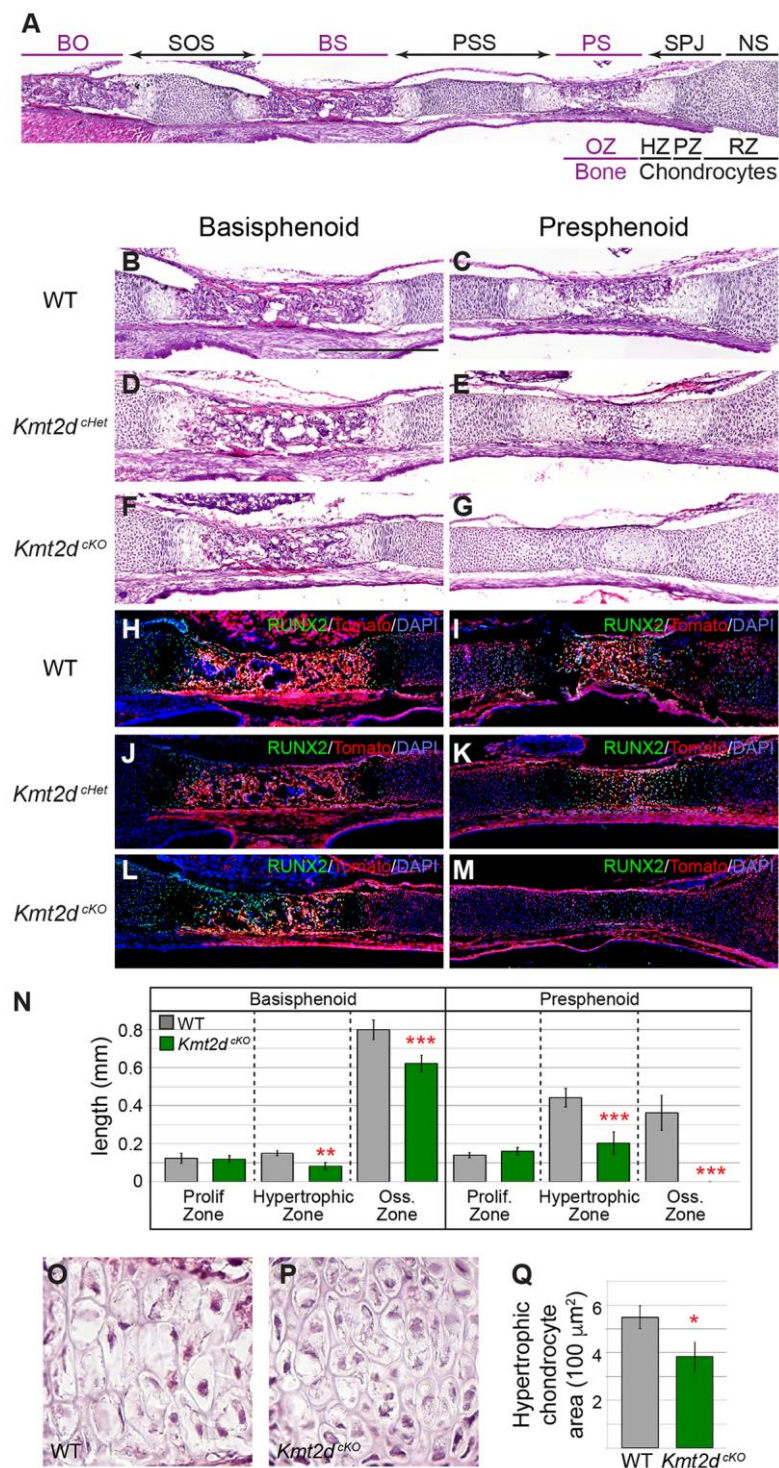


Figure 7: Analysis of *Kmt2d*^{CKO} function in cranial base endochondral ossification. (A) Low magnification view of H&E stained P1 sagittal section through the midline of the WT cranial base. Illustrated in purple are the ossification zones for the BO: basioccipital bone, BS: basisphenoid bone, and PS: presphenoid bone. Illustrated in black are the cartilage growth zones (arrow heads for growth direction) for the SOS:

spheno-occipital synchondrosis, PSS: presphenoidal synchondrosis, and SPJ: septopresphenoidal junction arising from the NS: nasal septum. Below the image is an annotated example of chondrocyte RZ: resting zone, PZ: proliferative zone, and HZ: hypertrophic zone that leads to bone growth in the OZ: ossification zone. (B-G) Higher magnification images of H&E stained sagittal sections of WT, *Kmt2d^{ch}*, or *Kmt2d^{cko}* basisphenoid (left) or presphenoid (right) ossification centers with surrounding differentiating chondrocyte growth zones. Black scale bar in B = 0.5 mm. (H-M) Basisphenoid (left) or Presphenoid (right) ossification regions with NCC based tomato reporter fluorescence in WT, *Kmt2d^{ch}* or *Kmt2d^{cko}* sections driven by *Wnt1-Cre*. Lower-level RUNX2 immunofluorescence labels proliferative and differentiating hypertrophic chondrocytes while higher-level RUNX2 expression labels osteoblasts. (N) Sagittal section length quantitation of WT or *Kmt2d^{cko}* zones of chondrocyte proliferation, hypertrophic chondrocyte differentiation, or bone ossification. WT presphenoid hypertrophic zones were measured on both sides of the ossification zone and added together. N ≥ 4. (O-P) High magnification H&E stained sagittal sections of presphenoidal WT and *Kmt2d^{cko}* hypertrophic chondrocytes from part C and G. (Q) Quantified hypertrophic chondrocyte cellular area. N = 3: averages for cellular area from all hypertrophic chondrocytes in the midline section was used as a single biological replicate.

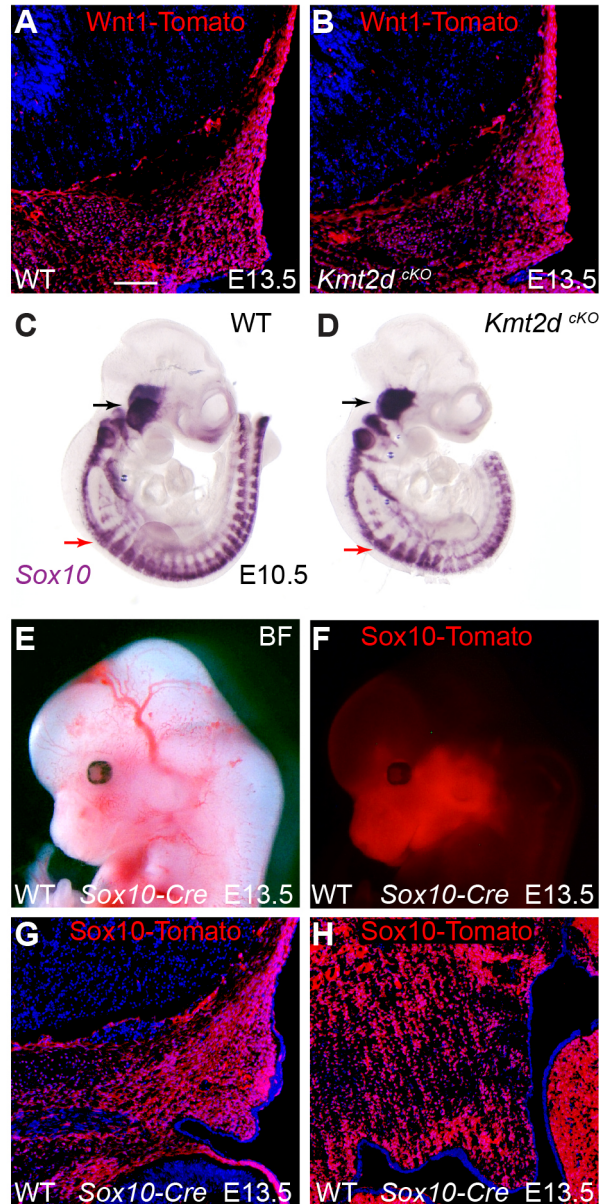
Figure S1

Figure S1: Localization of *Wnt1-Cre* and *Sox10-Cre* recombination domains and *Sox10* expression in *Kmt2d^{cKO}* embryos. (A-B) E13.5 WT and *Kmt2d^{cKO}* coronal sections of supraorbital frontal primordia indicating *Wnt1-Cre* driven tomato reporter fluorescence. White scale bar in A = 0.1 mm. (C-D) Whole mount RNA *in situ* hybridization for *Sox10* in WT and *Kmt2d^{cKO}* E10.5 embryos. Black arrows indicate post-migratory NCC localization to trigeminal ganglia and red arrows depict dorsal root ganglia. (E-F) Bright field (BF) and tomato fluorescent images of NCC lineage tracing in WT E13.5 *Sox10-Cre* embryos. (G-H) Coronal sections through WT E13.5 *Sox10-Cre* supraorbital ridge (G) and palatal shelf (H) indicating efficient tomato reporter activity in NCCs from these regions.

Figure S2

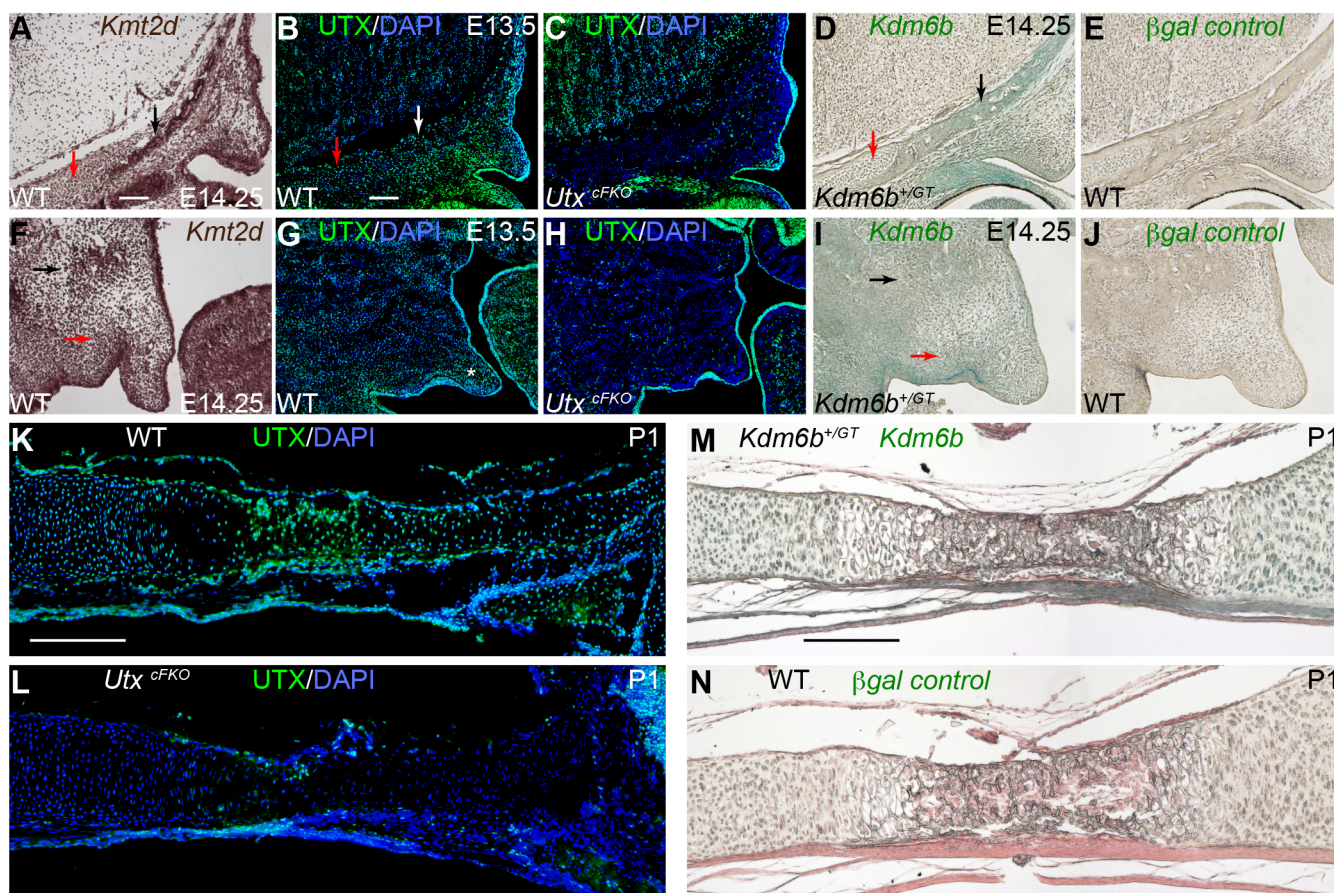


Figure S2: Expression patterns of *Kmt2d*, *Utx*, and *Kdm6b* in NCCs. (A-E) Expression in supraorbital frontal primordia. White scale bars in A and B = 0.1 mm. *Kmt2d* expression was analyzed by RNA *in situ* hybridization (A). UTX immunofluorescence was performed (B) with *Utx^{cFKO}* tissue serving as negative control (C). *Kdm6b* expression was analyzed by X-Gal staining of a heterozygous *Kdm6b* gene trap (*Kdm6b^{+/-GT}*) that fuses the transcript with β -galactosidase (D). WT sections served as control for the β -galactosidase assay (E). Black and white arrows in A-E denote osteoblasts while red arrows denote chondrocytes. (F-J) Expression patterns of *Kmt2d*, *Utx*, and *Kdm6b* in coronal palatal shelves with staining as indicated in parts A-E. Black arrows highlight osteoblast differentiation, red arrows depict subepithelial mesenchymal expression, and the white asterisk illustrated expression in the distal palatal tip. (K-N) Expression patterns of *Utx* and *Kdm6b* in sagittal presphenoid regions of the P1 cranial base with staining as indicated in parts B-E. White and black scale bars in K and M = 0.2 mm.

Figure S3

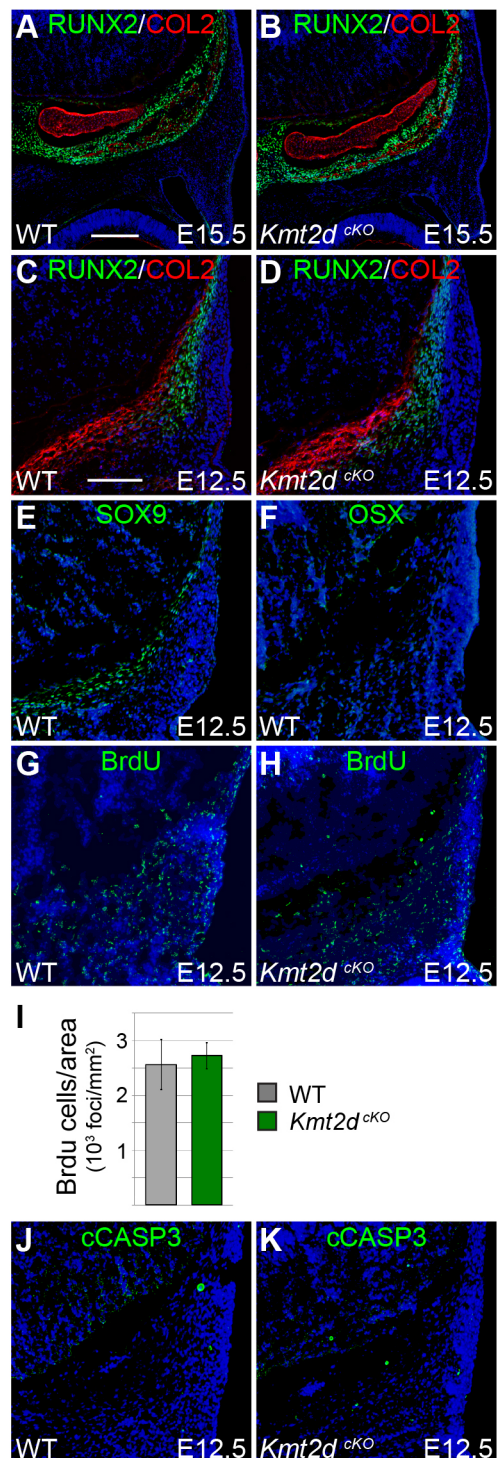


Figure S3: Cellular phenotypes in *Kmt2d^{cko}* supraorbital frontal primordia. (A-B) Osteoblast (RUNX2+) or chondrocyte (COL2+) domains in E15.5 WT or *Kmt2d^{cko}* frontal coronal sections. White scale bar in A = 0.2 mm. (C-D) Pre-osteoblast (RUNX2+) or pre-chondrocytes (COL2+) in E12.5 WT or *Kmt2d^{cko}* coronal sections of frontal primordia. White scale bar in C = 0.1 mm. (E) SOX9+ pre-chondrocytes in E12.5 WT coronal sections of frontal primordia. (F) E12.5 pre-osteoblasts do not express OSX. (G-H) E12.5 WT and *Kmt2d^{cko}* embryos were labeled with BrdU for 2 hours and detected by immunofluorescence. (I) E12.5 BrdU positive cells were counted from osteoblast regions (identified in parts C-D) and normalized to area scored. N ≥ 4 supraorbital osteoblast domains averaged from 3 sections spaced 60 microns apart. (J-K) Apoptotic cells were identified in E12.5 WT or *Kmt2d^{cko}* frontal primordia by immunofluorescence for active cleaved Caspase 3.

Figure S4

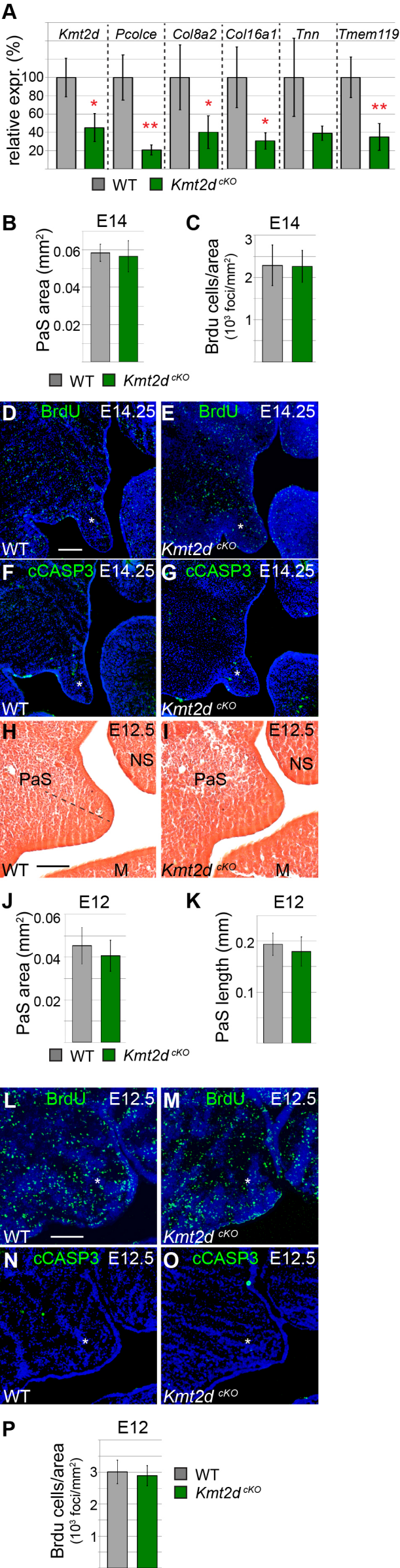


Figure S4: Cellular phenotypes in *Kmt2d^{cko}* palatal shelves. (A) qRT-PCR verification of genes identified in E14.25 *Kmt2d^{cko}* palatal shelf RNA-seq. (B) The area of the distal palatal shelf (PaS) tip indicated in Figure 5J-K was measured. N = 3 sets of palatal shelf distal tip measurements averaged from 2 anterior-central sections spaced 80 microns apart. (C) E14.25 WT and *Kmt2d^{cko}* embryos were labeled with BrdU for 2 hours and detected by immunofluorescence (D-E). White scale bar in D = 0.1 mm. BrdU positive cells were counted from the distal palatal tip (white asterisks) and plotted normalized to area scored (C). N = 4 sets of palatal shelf distal tip measurements averaged from 2 anterior-central sections spaced 80 microns apart. (F-G) Apoptotic cells were identified in E142.5 WT or *Kmt2d^{cko}* distal palatal extensions (white asterisks) by immunofluorescence for active cleaved Caspase 3. (H-I) Picrosirius red staining of E12.5 WT and *Kmt2d^{cko}* palatal outgrowths. Dashed line indicates region measured in part K. Black scale bar in H = 0.1 mm. (J-K) Measured area (J) and length (K) of the *Kmt2d^{cko}* palatal outgrowth indicated in parts H-I. Anterior to middle palatal sections were scored and quantified. N ≥ 7 sets of palatal shelf outgrowth measurements scored and quantified from anterior-central sections demonstrating the largest measurements. (L-M) E12.5 WT and *Kmt2d^{cko}* embryos were labeled with BrdU for 2 hours and detected by immunofluorescence in palatal outgrowths (white asterisks). White scale bar in L = 0.1 mm. (N-O) Apoptotic cells were identified in E12.5 WT or *Kmt2d^{cko}* palatal outgrowths by immunofluorescence for active cleaved Caspase 3. (P) BrdU positive cells were counted from the E12.5 anterior palatal outgrowths (white asterisks in parts L-M) and plotted normalized to area scored. N = 4 palatal shelf outgrowth measurements averaged from 2 anterior-central sections spaced 60 microns apart.

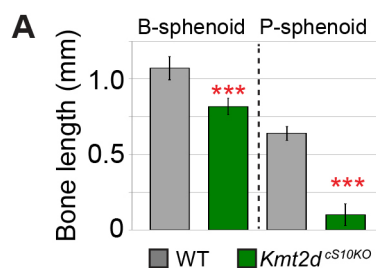
Figure S5

Figure S5: $Kmt2d^{cS10KO}$ cranial base quantitation. (A) Basisphenoid (B-sphenoid) and presphenoid (P-sphenoid) bone lengths were imaged and measured from whole mount alizarin red and alcian blue skeletal preparations in P1 WT and $Kmt2d^{cS10KO}$ pups. $N \geq 4$.

Table S1: Differential gene expression analysis for RNA-seq on E14.25 WT and *Kmt2d^{cko}* palatal shelves. Sheet 1: Significantly downregulated genes (FDR < 0.05) in *Kmt2d^{cko}* palatal shelves. Sheet 2: Significantly upregulated genes (FDR < 0.05) in *Kmt2d^{cko}* palatal shelves. Sheet 3: *Kmt2d^{cko}* downregulated genes from sheet 1 with elevated WT expression (RPKM > 2) and greater fold change (*Kmt2d^{cko}* logFC < -1). Sheet 4: Extracellular matrix components identified by MSigDB or IPA pathway analysis that were downregulated in *Kmt2d^{cko}* palatal shelves.

[Click here to Download Table S1](#)

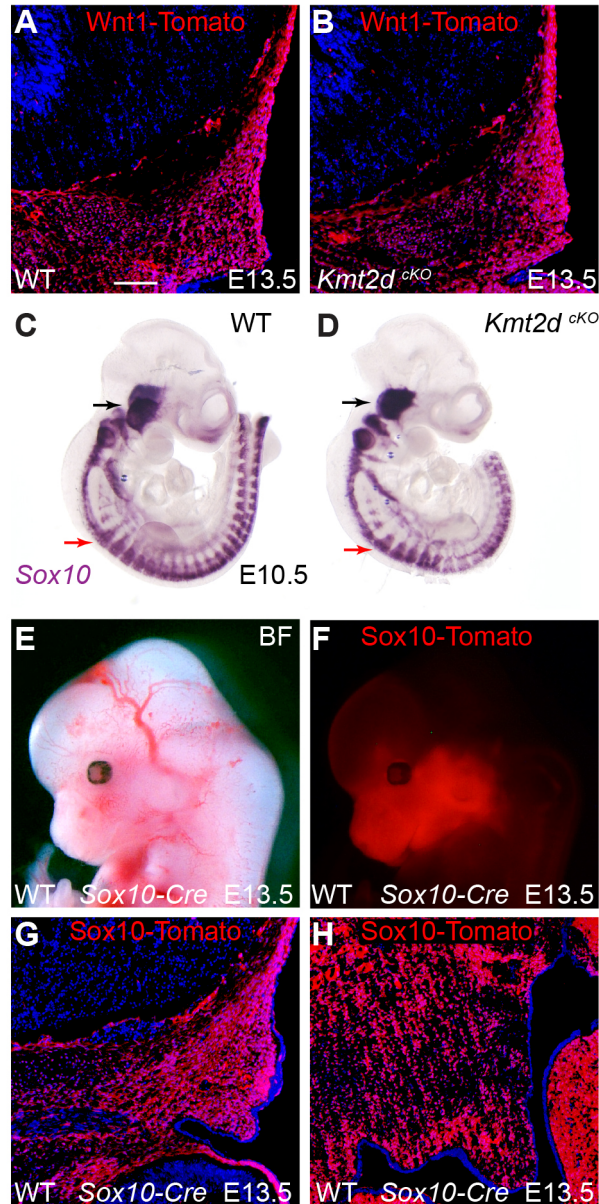
Figure S1

Figure S1: Localization of *Wnt1*-Cre and *Sox10*-Cre recombination domains and *Sox10* expression in *Kmt2d*^{cKO} embryos. (A-B) E13.5 WT and *Kmt2d*^{cKO} coronal sections of supraorbital frontal primordia indicating *Wnt1*-Cre driven tomato reporter fluorescence. White scale bar in A = 0.1 mm. (C-D) Whole mount RNA *in situ* hybridization for *Sox10* in WT and *Kmt2d*^{cKO} E10.5 embryos. Black arrows indicate post-migratory NCC localization to trigeminal ganglia and red arrows depict dorsal root ganglia. (E-F) Bright field (BF) and tomato fluorescent images of NCC lineage tracing in WT E13.5 *Sox10*-Cre embryos. (G-H) Coronal sections through WT E13.5 *Sox10*-Cre supraorbital ridge (G) and palatal shelf (H) indicating efficient tomato reporter activity in NCCs from these regions.

Figure S2

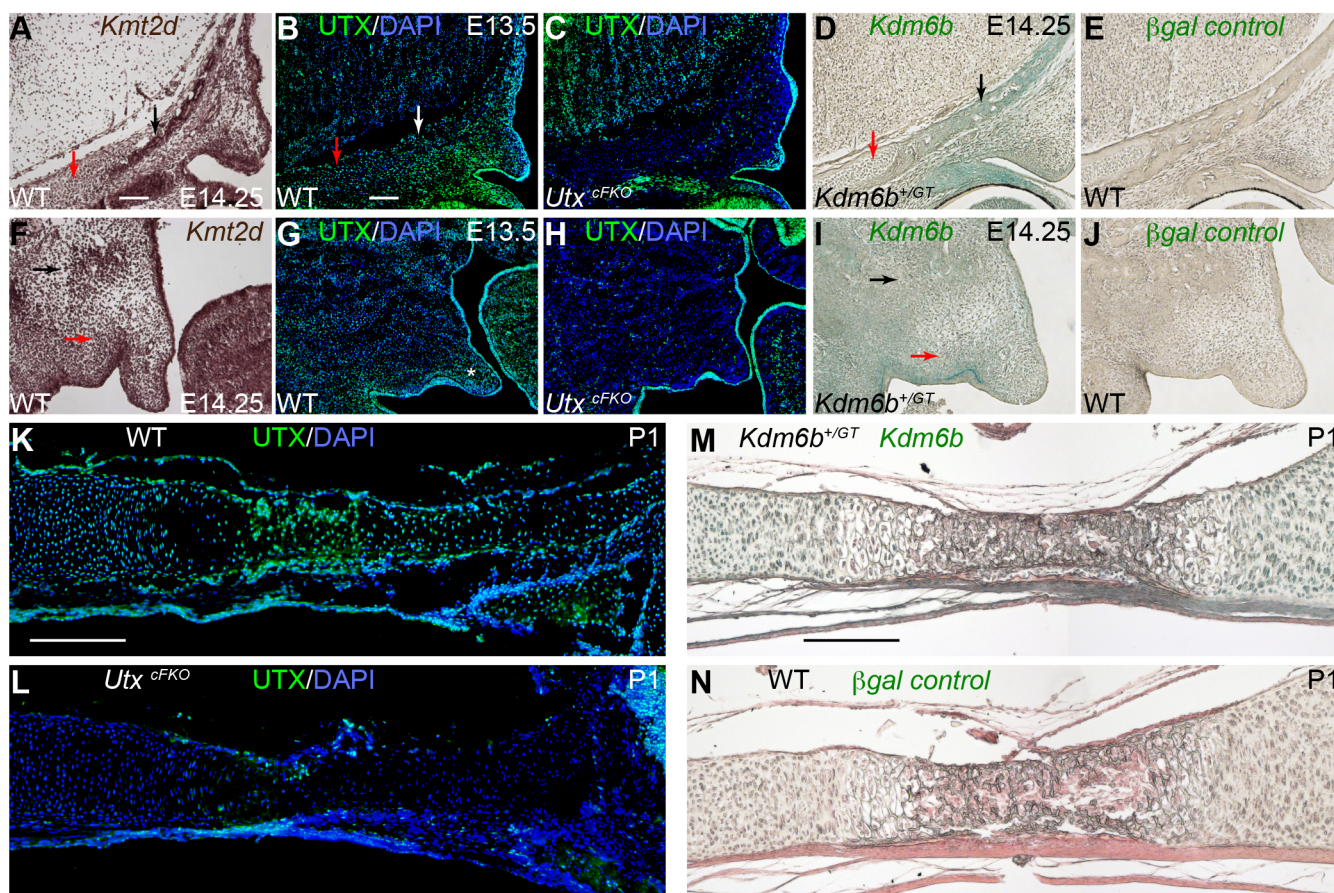


Figure S2: Expression patterns of *Kmt2d*, *Utx*, and *Kdm6b* in NCCs. (A-E) Expression in supraorbital frontal primordia. White scale bars in A and B = 0.1 mm. *Kmt2d* expression was analyzed by RNA *in situ* hybridization (A). UTX immunofluorescence was performed (B) with *Utx*^{cFKO} tissue serving as negative control (C). *Kdm6b* expression was analyzed by X-Gal staining of a heterozygous *Kdm6b* gene trap (*Kdm6b*^{+/_{GT}}) that fuses the transcript with β-galactosidase (D). WT sections served as control for the β-galactosidase assay (E). Black and white arrows in A-E denote osteoblasts while red arrows denote chondrocytes. (F-J) Expression patterns of *Kmt2d*, *Utx*, and *Kdm6b* in coronal palatal shelves with staining as indicated in parts A-E. Black arrows highlight osteoblast differentiation, red arrows depict subepithelial mesenchymal expression, and the white asterisk illustrated expression in the distal palatal tip. (K-N) Expression patterns of *Utx* and *Kdm6b* in sagittal presphenoid regions of the P1 cranial base with staining as indicated in parts B-E. White and black scale bars in K and M = 0.2 mm.

Figure S3

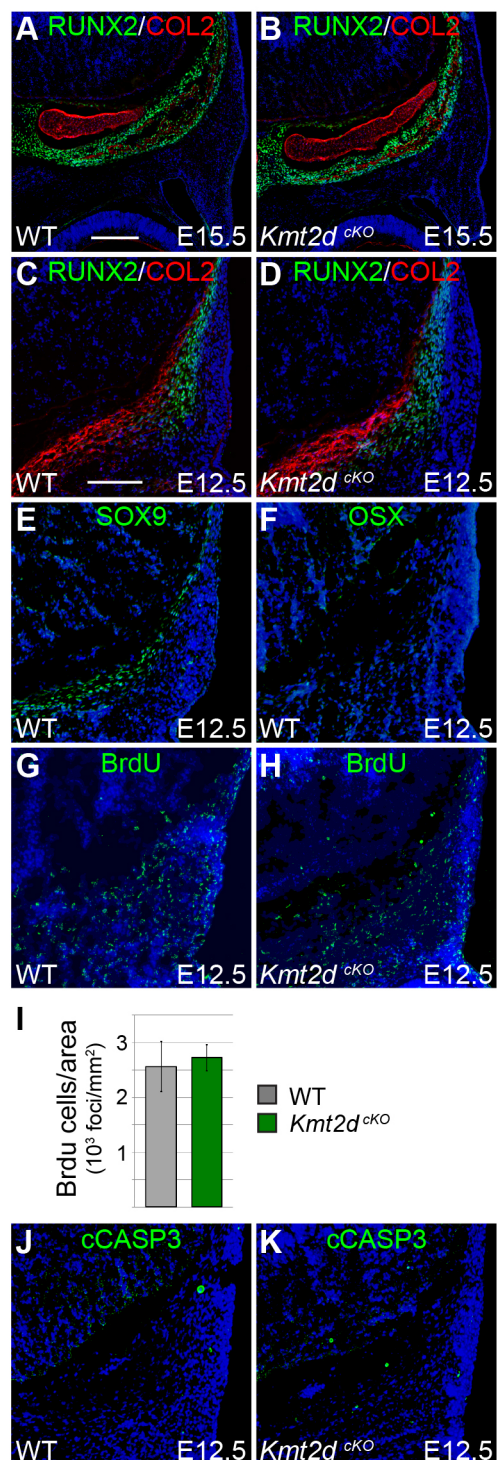


Figure S3: Cellular phenotypes in *Kmt2d^{cko}* supraorbital frontal primordia. (A-B) Osteoblast (RUNX2+) or chondrocyte (COL2+) domains in E15.5 WT or *Kmt2d^{cko}* frontal coronal sections. White scale bar in A = 0.2 mm. (C-D) Pre-osteoblast (RUNX2+) or pre-chondrocytes (COL2+) in E12.5 WT or *Kmt2d^{cko}* coronal sections of frontal primordia. White scale bar in C = 0.1 mm. (E) SOX9+ pre-chondrocytes in E12.5 WT coronal sections of frontal primordia. (F) E12.5 pre-osteoblasts do not express OSX. (G-H) E12.5 WT and *Kmt2d^{cko}* embryos were labeled with BrdU for 2 hours and detected by immunofluorescence. (I) E12.5 BrdU positive cells were counted from osteoblast regions (identified in parts C-D) and normalized to area scored. N ≥ 4 supraorbital osteoblast domains averaged from 3 sections spaced 60 microns apart. (J-K) Apoptotic cells were identified in E12.5 WT or *Kmt2d^{cko}* frontal primordia by immunofluorescence for active cleaved Caspase 3.

Figure S4

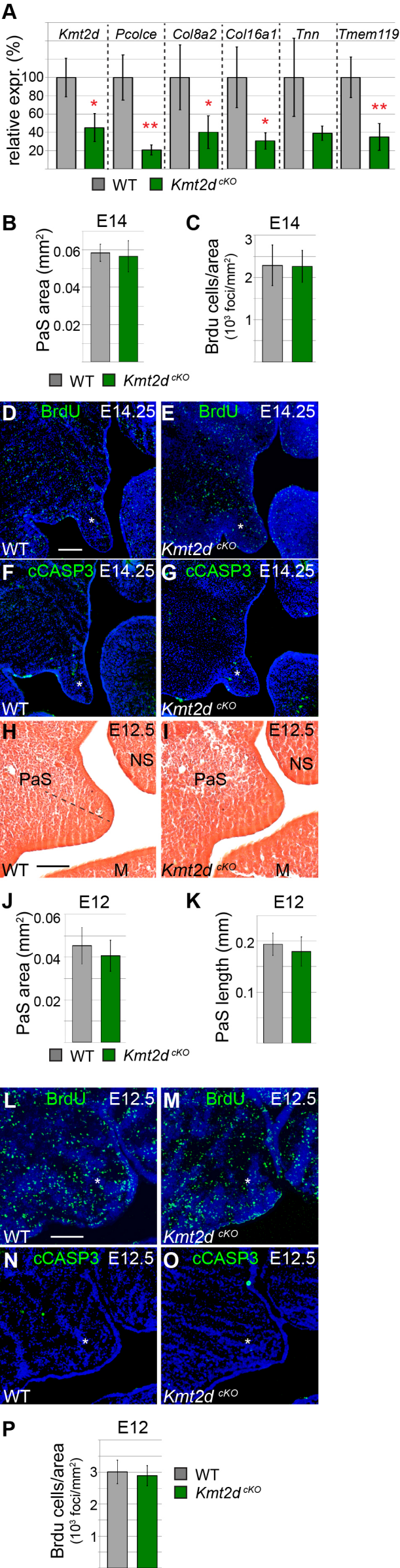


Figure S4: Cellular phenotypes in *Kmt2d^{cko}* palatal shelves. (A) qRT-PCR verification of genes identified in E14.25 *Kmt2d^{cko}* palatal shelf RNA-seq. (B) The area of the distal palatal shelf (PaS) tip indicated in Figure 5J-K was measured. N = 3 sets of palatal shelf distal tip measurements averaged from 2 anterior-central sections spaced 80 microns apart. (C) E14.25 WT and *Kmt2d^{cko}* embryos were labeled with BrdU for 2 hours and detected by immunofluorescence (D-E). White scale bar in D = 0.1 mm. BrdU positive cells were counted from the distal palatal tip (white asterisks) and plotted normalized to area scored (C). N = 4 sets of palatal shelf distal tip measurements averaged from 2 anterior-central sections spaced 80 microns apart. (F-G) Apoptotic cells were identified in E142.5 WT or *Kmt2d^{cko}* distal palatal extensions (white asterisks) by immunofluorescence for active cleaved Caspase 3. (H-I) Picrosirius red staining of E12.5 WT and *Kmt2d^{cko}* palatal outgrowths. Dashed line indicates region measured in part K. Black scale bar in H = 0.1 mm. (J-K) Measured area (J) and length (K) of the *Kmt2d^{cko}* palatal outgrowth indicated in parts H-I. Anterior to middle palatal sections were scored and quantified. N ≥ 7 sets of palatal shelf outgrowth measurements scored and quantified from anterior-central sections demonstrating the largest measurements. (L-M) E12.5 WT and *Kmt2d^{cko}* embryos were labeled with BrdU for 2 hours and detected by immunofluorescence in palatal outgrowths (white asterisks). White scale bar in L = 0.1 mm. (N-O) Apoptotic cells were identified in E12.5 WT or *Kmt2d^{cko}* palatal outgrowths by immunofluorescence for active cleaved Caspase 3. (P) BrdU positive cells were counted from the E12.5 anterior palatal outgrowths (white asterisks in parts L-M) and plotted normalized to area scored. N = 4 palatal shelf outgrowth measurements averaged from 2 anterior-central sections spaced 60 microns apart.

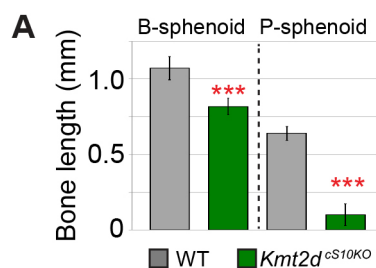
Figure S5

Figure S5: $Kmt2d^{cS10KO}$ cranial base quantitation. (A) Basisphenoid (B-sphenoid) and presphenoid (P-sphenoid) bone lengths were imaged and measured from whole mount alizarin red and alcian blue skeletal preparations in P1 WT and $Kmt2d^{cS10KO}$ pups. $N \geq 4$.

Table S1: Differential gene expression analysis for RNA-seq on E14.25 WT and *Kmt2d^{cko}* palatal shelves. Sheet 1: Significantly downregulated genes (FDR < 0.05) in *Kmt2d^{cko}* palatal shelves. Sheet 2: Significantly upregulated genes (FDR < 0.05) in *Kmt2d^{cko}* palatal shelves. Sheet 3: *Kmt2d^{cko}* downregulated genes from sheet 1 with elevated WT expression (RPKM > 2) and greater fold change (*Kmt2d^{cko}* logFC < -1). Sheet 4: Extracellular matrix components identified by MSigDB or IPA pathway analysis that were downregulated in *Kmt2d^{cko}* palatal shelves.

[Click here to Download Table S1](#)

Table S2: Genotyping and qRT-PCR primers used in this study.

[Click here to Download Table S2](#)